(2)

PICOSECOND LASER BREAKDOWN THRESHOLDS IN GASES

AFOSR 86-0317

Final Scientific Report

Dennis Keefer, PhD
Principal Investigator

University of Tennessee Space Institute
Center for Laser Applications
Tullahoma, TN 37388-8897

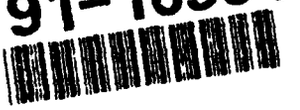

REPORT DOCUMENTATION PAGE

Form Approved OMB No. 0704-0188

a. REPORT SECURITY CLASSIFICATION: Unclassified

1b. RESTRICTIVE MARKINGS:

2a. SECURITY CLASSIFICATION AUTHORITY:

2b. DECLASSIFICATION / DOWNGRADING SCHEDULE:

3. DISTRIBUTION / AVAILABILITY OF REPORT: Approved for public release; distribution is unlimited.

4. PERFORMING ORGANIZATION REPORT NUMBER(S):

5. MONITORING ORGANIZATION REPORT NUMBER(S):

6a. NAME OF PERFORMING ORGANIZATION: University of Tennessee Space Institute

6b. OFFICE SYMBOL (If applicable): CLA

7a. NAME OF MONITORING ORGANIZATION: AFOSR/NA

6c. ADDRESS (City, State, and ZIP Code): Center for Laser Applications MS-14 B.H. Goethert Pkwy. Tullahoma, TN 37388-8897

7b. ADDRESS (City, State, and ZIP Code): Building 410, Bolling AFB DC 20332-6448

8a. NAME OF FUNDING / SPONSORING ORGANIZATION: AFOSR/NA

8b. OFFICE SYMBOL (If applicable): NA

9. PROCUREMENT INSTRUMENT IDENTIFICATION NUMBER: AFOSR-86-0317

8c. ADDRESS (City, State, and ZIP Code): Building 410, Bolling AFB DC 20332-6448

10. SOURCE OF FUNDING NUMBERS

PROGRAM ELEMENT NO.	PROJECT NO.	TASK NO.	WORK UNIT ACCESSION NO.
61102F	2308	A1	

11. TITLE (Include Security Classification): (U) Picosecond Laser Breakdown Thresholds in Gases

12. PERSONAL AUTHOR(S): Dr. Dennis Keefer

13a. TYPE OF REPORT	13b. TIME COVERED	14. DATE OF REPORT (Year, Month, Day)	15. PAGE COUNT
Final Scientific	FROM 2/28/90 TO 9/30/91	1991 September 30	13

16. SUPPLEMENTARY NOTATION:

17. COSATI CODES			18. SUBJECT TERMS (Continue on reverse if necessary and identify by block number)
FIELD	GROUP	SUB-GROUP	Optical Breakdown, Picosecond laser pulses, laser propulsion, laser sustained plasmas, plasma spectroscopy, argon plasmas, optical plasmotron, free electron lasers

19. ABSTRACT (Continue on reverse if necessary and identify by block number)

see paper

20. DISTRIBUTION / AVAILABILITY OF ABSTRACT: ☒ UNCLASSIFIED/UNLIMITED ☒ SAME AS RPT. ☐ DTIC USERS

21. ABSTRACT SECURITY CLASSIFICATION: Unclassified

22a. NAME OF RESPONSIBLE INDIVIDUAL: Dr. Mitat Birkan

22b. TELEPHONE (Include Area Code): (202) 767-4935

22c. OFFICE SYMBOL: AFOSR/NA

DD Form 1473, JUN 86 Previous editions are obsolete. SECURITY CLASSIFICATION OF THIS PAGE

PICOSECOND LASER BREAKDOWN THRESHOLDS IN GASES

Contract AFOSR-86-0317

FINAL REPORT

Dennis Keefer, PhD
Principal Investigator

I. INTRODUCTION

An experimental investigation of laser sustained plasmas (LSP) was begun in 1984 at The University of Tennessee Space Institute (UTSI). The objective of this research was to understand the basic physical mechanisms of the LSP and determine their influence on stability, laser power absorption, thermal radiation loss and thermal conversion efficiency. The approach used was to create the LSP in argon using a continuous wave (CW) carbon dioxide laser at moderate powers (1.5 kW) and to obtain detailed measurements of the plasma temperature field by using a modern digital image processing computer to acquire spectral images of the plasma emission. Using the measured temperature field, the laser power absorption and thermal plasma emission could be calculated at any point within the LSP to provide a detailed understanding of the energy conversion processes.

These experiments provided an answer to the crucial question concerning the stability of the LSP in a forced convective flow, and an understanding of the basic physical mechanisms which is required for control of the thermal radiation loss from the plasma and the fractional absorption of the laser beam. The principal results that were obtained from these experiments are:

1. The LSP is stable in the presence of forced convective flow for incident flow velocities of at least 8 m/s.

2. The structure of the LSP depends critically on the incident flow velocity, the pressure and the optical configuration used to sustain the plasma.

3. The incident flow velocity can be used to control the position and shape of the plasma within the focal volume.

These results indicate that there are no "fatal flaws" in the concept utilizing the LSP for laser thermal propulsion, and suggest that the internal energy conversion processes can be sufficiently well controlled through the optical and flow configurations to provide an efficient, high specific impulse propulsion system.

The initial results of the UTSI and other experiments, together with the development of detailed computational codes, make the prospect for a practical laser propulsion system

appear highly favorable. Implementation of an operational beamed laser propulsion system will depend, of course, on the availability of lasers having sufficient power, in the range from 1 to 1000 MW. Recent developments in high power lasers instigated by the Strategic Defense Initiative (SDI) appear to favor the free electron laser (FEL) for high power applications.

The characteristics of the free electron laser are considerably different than the CW carbon dioxide lasers that have been used for the previous experimental research on laser sustained plasmas. The FEL does not have a continuous power output, but produces its output as a series of short pulses with high peak power and a duty cycle of 0.001 or less. The physical processes associated with the absorption of short optical pulses by an absorbing plasma are considerably different than for a CW laser, and these processes must be understood in order to evaluate the prospects for beamed laser propulsion using high power free electron lasers.

Experiments were performed by UTSI at Los Alamos National Laboratory (LANL) in August, 1988 to study quasi-steady plasmas sustained with the beam from a RF Linac free electron laser. This laser produced a train of pulses having a wavelength of 10.6 micrometers with a pulse width of 10 ps. These pulses were separated by 46 ns, and each pulse train consisted of approximately 1730 pulses. The total energy in the pulse train ranged from 10 to 200 mJ. Argon plasmas were easily initiated and sustained with this laser, and spectroscopic data were obtained which verified their quasi-steady nature. Spectroscopic measurements gave temperatures of 17,000 to 20,000 K, similar to that observed in plasmas sustained with continuous wave carbon dioxide lasers. Numerous attempts were also made to initiate and sustain similar plasmas in hydrogen and in nitrogen, but these were unsuccessful. The details of this experiment can be found in a paper which has been accepted for publication in the AIAA Journal of Propulsion and Power, and is included as Appendix A of this report.

Further experiments designed to understand the development of plasma breakdown using picosecond optical pulses were undertaken in our laboratory at UTSI. The combination of 10 ps pulse duration at a wavelength of 10.6 micrometers was unique to the LANL laser, and so these experiments were performed using 532 nm radiation from a frequency doubled Nd:YAG laser. A laser collinear pump-probe diagnostic technique was developed that permitted observation of the pre-breakdown plasma with a time resolution of 3 ps. This work was presented at the CLEO meeting held in Baltimore, Maryland, May 12-17, 1991 [1]. A paper describing this work in detail will be submitted to the Journal of Applied Physics, and a preprint of the manuscript is included as Appendix B to this report.

Detailed theoretical models were developed at UTSI in an attempt to understand the failure to initiate plasmas in the molecular gases driven using the beam from a FEL. Because of the picosecond time scales involved, the electron distribution function is far from equilibrium during the laser pulse. A computational code was developed which uses a one-dimensional particle-in-cell (PIC) method to calculate the electron distribution function, electron and ion densities and the resulting electric field. A Monte Carlo method was used to include the effects of elastic and inelastic collisions. The gas in the focal volume is

heated during the 46 ns time between laser micropulses as elastic collisions relax the electron energy. There are two important effects that result from this relaxation during the time between pulses. If the average electron temperature relaxes rapidly enough it will allow significant reduction of electron density by 3-body recombination, and the energy gained from the electrons by the heavy species can result in a gasdynamic expansion of the focal volume. A set of coupled rate equations were used to calculate the rate of relaxation and the reduction of electron density, and gasdynamic expansion of this heated gas was calculated using a one-dimensional CFD code.

The results of the theoretical models indicate that the breakdown in the FEL experiments did not occur during a single 10 picosecond pulse, but was the result of a cumulative growth of the electron density resulting from the absorption of approximately 8 pulses in argon. The code also indicates that hydrogen and nitrogen did not reach breakdown because of a faster decay of electron energy in these gases during the 46 ns time between pulses. This faster decay rate occurs because of inelastic vibrational collisions and more rapid energy loss in inelastic collisions due to the smaller mass of the hydrogen and nitrogen molecules. There may also be an effect due to the different behavior of the argon electron-neutral collision cross section with electron energy. The energy loss, in itself, does not prevent a buildup of electron density to breakdown threshold, but the lower electron energy results in a much faster electron recombination rate which depletes the electron density between pulses.

The theoretical code development is the basis of a PhD dissertation that is being written by Ms. Quan Zhang, and will be submitted during the Spring semester of 1992. A technical paper describing this theoretical model in detail will soon be prepared and submitted for presentation and publication. A more detailed description of the theoretical model will also be presented in the next section.

II. THEORETICAL MODEL FOR PICOSECOND BREAKDOWN

A theoretical model was developed in an attempt to understand why plasma breakdown in argon could be easily initiated using the Los Alamos FEL, but plasma breakdown could not be achieved using either hydrogen or nitrogen. Earlier theoretical studies indicated that the breakdown threshold for these gases should be similar, but these calculations were made for a single 10 ps laser pulse. It was suspected that breakdown did not occur during a single FEL laser pulse, but occurred because of an accumulation of electron density which occurred over several successive 10 ps pulses. A computational code was developed which supported that hypothesis and predicted the disparity in breakdown that was observed among the three gases attempted.

A. Model Description

The most important feature of the processes leading to the plasma breakdown produced by a picosecond laser pulse is the strongly non-Maxwellian electron distribution function produced during the pulse. For the breakdown in gases at a

pressure of one atmosphere, the electron-neutral collision frequency is approximately 1 ps. Therefore, an electron will experience only about 10 collisions during the 10 ps pulse duration. This collision frequency is insufficient to enforce a Maxwellian distribution of electron energy during the pulse duration, but can lead to large electron energies.

Boltzmann's equation describes the time evolution of the electron energy distribution, and we developed a model which allows an approximate solution to be obtained. As an initial electron in the focal volume of the laser absorbs energy from the optical electric field, the electron undergoes oscillation at the optical frequency until it suffers a collision with a neutral particle. This oscillation is in the direction of the electric field and is referred to as the "quiver energy". Due to the large difference between the electron and the neutral particle masses the electron will change its direction, on the average, by 90 degrees upon collision with a neutral atom [2]. After the collision, the electron again begins to oscillate in the direction of the electric field, while retaining the energy it had gained prior to collision. In this way the electron rapidly increases its energy with each elastic electron-neutral collision.

The model attempts to describe the evolution of the electron distribution function from a single electron placed in the focal volume until electron ionizing collisions have produced an avalanche of electrons that reaches plasma breakdown. Breakdown is assumed to occur when the electron density reaches approximately $10^{17}cm^{-3}$. Since we are only concerned with the initial breakdown, we will assume that the electrons are confined to a spherical volume centered on the focal point of the laser beam. This permits a one-dimensional description of the problem. In the actual experimental breakdown, the plasma will rapidly extend along the laser beam into a long cylindrical plasma once breakdown has been achieved at the focal point.

The calculation begins with a single electron placed near the focal point. This electron undergoes elastic collisions until its energy exceeds that required to suffer an inelastic collision with a neutral molecule. This inelastic collision can result in an excited molecule, dissociation of the molecule into atoms, or an ionization event in which a second electron is produced. When a second electron is produced, it too gains energy from the optical electric field. In our computational model each electron is tracked in both space and time until the number of electrons reaches 60,000. Then, the number of electrons retained in the computation is reduced by a factor of approximately 3, and each computational electron now represents 3 real electrons. This process is repeated over a sequence of 10 ps laser pulses until no further increase in electron density occurs or the breakdown electron density is reached.

The electrons, having a small mass and a high energy, will attempt to diffuse out of the focal volume. However, their motion will be retarded by the positively charged heavy ions. Therefore, the ions and electrons will tend to diffuse together in ambipolar diffusion [2]. The resulting electric field is modeled using the PIC method [3]. The charge of each computational electron and ion is distributed onto

the spherical computational grid, and Poisson's equation is solved for this charge distribution to obtain the resulting electric field. In between collisions the electrons and ions move under the influence of this electric field. After each computational time step the charge is redistributed onto the computational grid and a new electric field is computed.

During the computational time step the electron trajectories are computed using the electric field calculated by the PIC method. At the same time, a Monte Carlo method is used to permit the particles to collide with ions and neutral particles with a probability determined by their energy dependent collision cross sections. Elastic, vibration, dissociation, excitation and ionizing collisions are all included. This procedure is followed during the 10 ps time the laser pulse is on, and for an additional 30 ps. During this 30 ps time the high energy electrons produced by the laser pulse continue to suffer ionizing collisions which further increase the electron density while reducing the average electron energy. The interval between the 10 ps laser pulses is 46 ns, and during this time the electrons continue to undergo mostly elastic collisions which slowly heat the neutral gas and further reduce the average electron energy.

If the average electron energy is significantly reduced during the time between pulses, then 3-body recombination of the electrons and ions may significantly reduce the electron density prior to the arrival of the next pulse. This effect can limit the cascade and lead to a saturation of electron number density at a level below breakdown threshold. A set of coupled rate equations for the electron number density and the average electron energy are solved during this 46 ns time period and used to establish the initial conditions for the subsequent 10 ps laser pulse. An additional effect of the elctron energy relaxation between pulses is the heating of the heavy gas within the focal volume.

After several pulses, when the electron density in the focal volume has reached approximately 10^{17} cm^{-3}, the gas heating between pulses is sufficient to produce a gasdynamic expansion which reduces the electron density prior to the arrival of the next pulse. This effect was computed using a one-dimensional gasdynamic code [4]. The computational electrons that remained from the prior pulse are reduced in number according to the reduction in density calculated from the gasdynamic code. Once the density has been reduced, the PIC process is repeated for the next laser pulse.

These computational steps: PIC calculation of the electric field, Monte Carlo calculation of collisions, and gasdynamic expansion are repeated for a sequence of 10 ps laser pulses until the electron number density saturates at a maximum value below breakdown or until breakdown is achieved. These calculations have been performed for the conditions of the Los Alamos experiments for argon, hydrogen and nitrogen.

B. Results and Conclusions

The calculated electron distribution function for argon during the fifth pulse in the sequence is shown in Figure 1. This figure plots the number of particles in the 10^{-7} cm^3 focal volume rather than the electron density. Note the relatively large number of electrons in the high energy tail of the distribution at 10 ps, the end of the laser pulse, and the relaxation of the distribution function to a more nearly Maxwellian form after 40 ps. A Maxwellian distribution having the same mean energy of 4.38 eV is also shown for comparison. The total number of electrons in the focal volume increases as the high energy electrons undergo ionizing collisions during the relaxation.

When the electron density reaches approximately 10^{17} cm^{-3}, enough energy is added to the gas through elastic collisions that gasdynamic expansion reduces the density in the focal volume. This gasdynamic expansion is calculated using a one-dimensional code, and the density ratio after pulse 8 is shown in Figure 2. The abscissa gives the computational grid location, and the edge of the laser beam is located at 250. For this pulse the density has been reduced to approximately one half by gasdynamic expansion during the 46 ns time between pulses.

The calculated electron density for argon and hydrogen is shown in Figure 3 for a sequence of ten pulses. The time scale between successive laser pulses has been contracted for clarity. It can be seen that argon reaches breakdown after 8 pulses. The electron number density in hydrogen reaches a plateau of approximately 10^{14} cm^{-3} after 6 pulses, and never achieves breakdown. This saturation effect is caused by a rapid recombination of electrons which occurs during the 46 ns between the laser pulses.

The 3-body recombination coefficient is a strong function of the electron temperature, and is largest for low energy electrons as shown in Figure 4. During the 46 ns between laser pulses the average electron energy decreases due to elastic and inelastic collisions between the electrons and neutrals. The rate of electron energy loss due to inelastic collisions is relatively small for argon because there are no vibrational or dissociation collisions, and the loss due to inelastic collisions is small because of the large atomic mass. The relaxation of the average energy in argon is shown in Figure 5. Since the electron energy remains relatively high during the 46 ns between pulses, recombination does not significantly reduce the electron density. On the other hand, vibration and dissociation collisions and a smaller molecular mass combine to rapidly reduce the electron energy between pulses for hydrogen and nitrogen. The relaxation of the average electron energy in hydrogen is shown in Figure 6 (note the difference in time scales). The reduced electron energy permits electron recombination to significantly reduce the electron density in the focal volume during the 46 ns between laser pulses. The result of this recombination is that, for hydrogen and nitrogen, the electron density saturates at a maximum value which is below plasma breakdown.

The original goal of this research was to determine whether quasi-steady plasmas, suitable for laser thermal propulsion, could be sustained with the pulsed laser beam from a free electron laser. Experiments conducted at Los Alamos National Laboratory confirmed that quasi-steady plasmas, with characteristics very similar to CW laser sustained plasmas, could be easily maintained in argon using the beam from their free electron laser. However, it was not possible to sustain quasi steady plasmas in hydrogen or nitrogen under the same conditions. A new pulse-probe laser diagnostic technique was developed at UTSI to measure the evolution of pre-breakdown laser induced plasmas with picosecond time resolution. Theoretical models were developed which predicts the breakdown disparity between argon and the molecular gases. The theory showed that electron recombination during the 46 ns between laser pulses prevented the multiple pulse cascade from reaching breakdown in the molecular gases.

These experiments confirm that high powered free electron lasers can be used to sustain quasi-steady plasmas that are suitable for laser thermal propulsion. The average power used in the LANL experiments was approximately 3 kW. This power is sufficient to sustain CW plasmas in argon using carbon dioxide lasers, but is insufficient to sustain hydrogen at the pressures used in these experiments. Therefore, it should also be possible to sustain quasi-steady plasmas in hydrogen, which is more suitable as a propellent, when sufficient average power is available in a free electron laser.

REFERENCES

1. L. M. Davis, L. Q. Li, D. Keefer and Q. Zhang, "Picosecond Resolved Evolution of Laser Breakdown in Gases," in Conference on Lasers and Electro-Optics, 1991 (Optical Society of America, Washington, D.C., 1991 pg. 462.

2. E. H. Holt and R. E. Haskell, Foundations of Plasma Dynamics, The McMacmillan Company, New York, 1965.

3. C. K. Birdsall and A. B. Langdon, Plasma Physics Via Computer Simulation, McGraw-Hill Book Company, 1985.

4. K. C. Hsieh, "Assessment of Numerical Techniques for Unsteady Flow Calculations," AIAA Computational Fluid Dynamics Conference, 9th, Buffalo, NY, June 13-15, 1989, technical paper A89-4177618-02 and Washington, DC, AIAA, 1989, p. 280-291, AIAA Paper #89-1956.

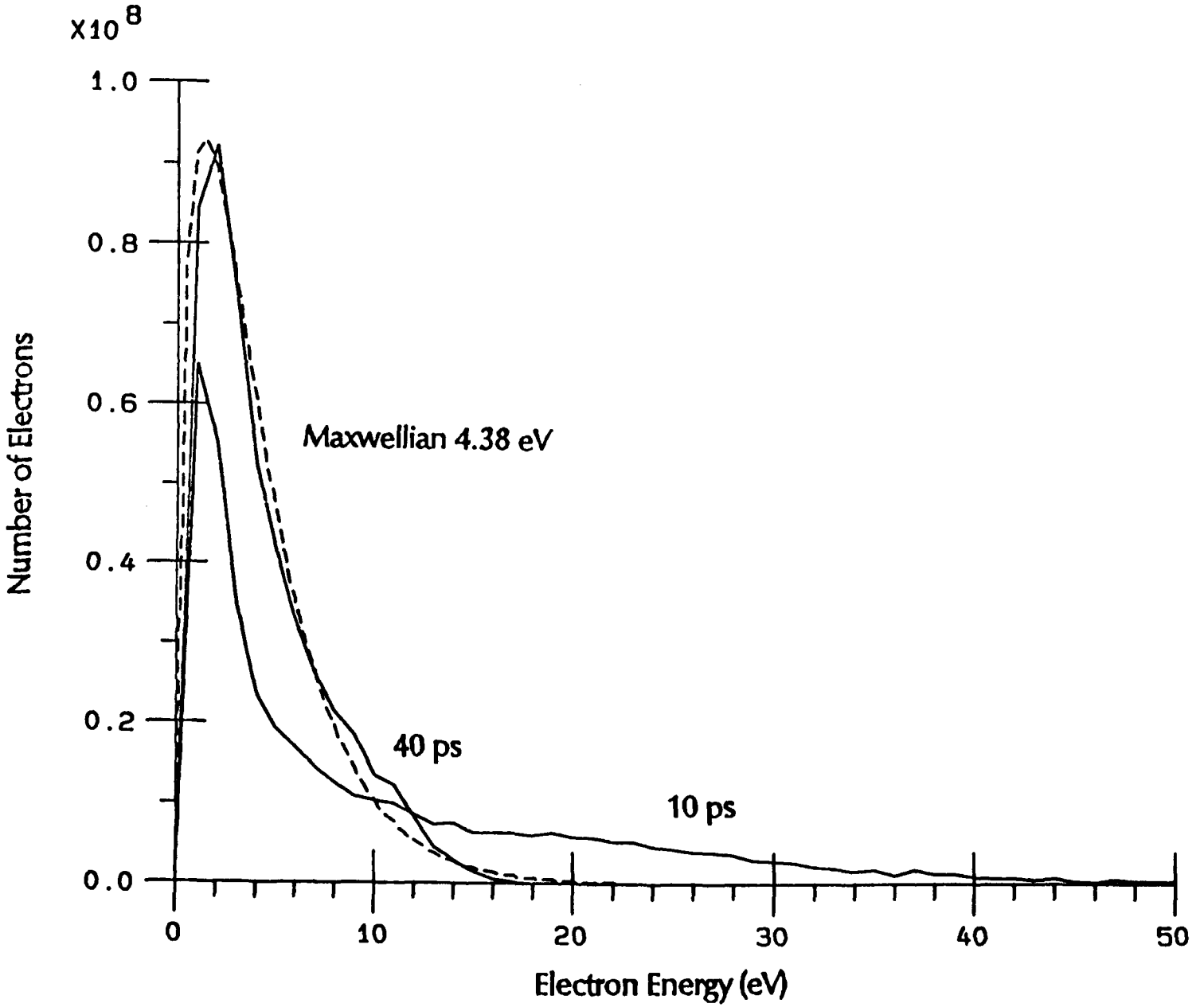

Figure 1. Electron distribution within focal volume at end of laser pulse (10 ps) and at 40 ps. Maxwellian distribution shown for comparison.

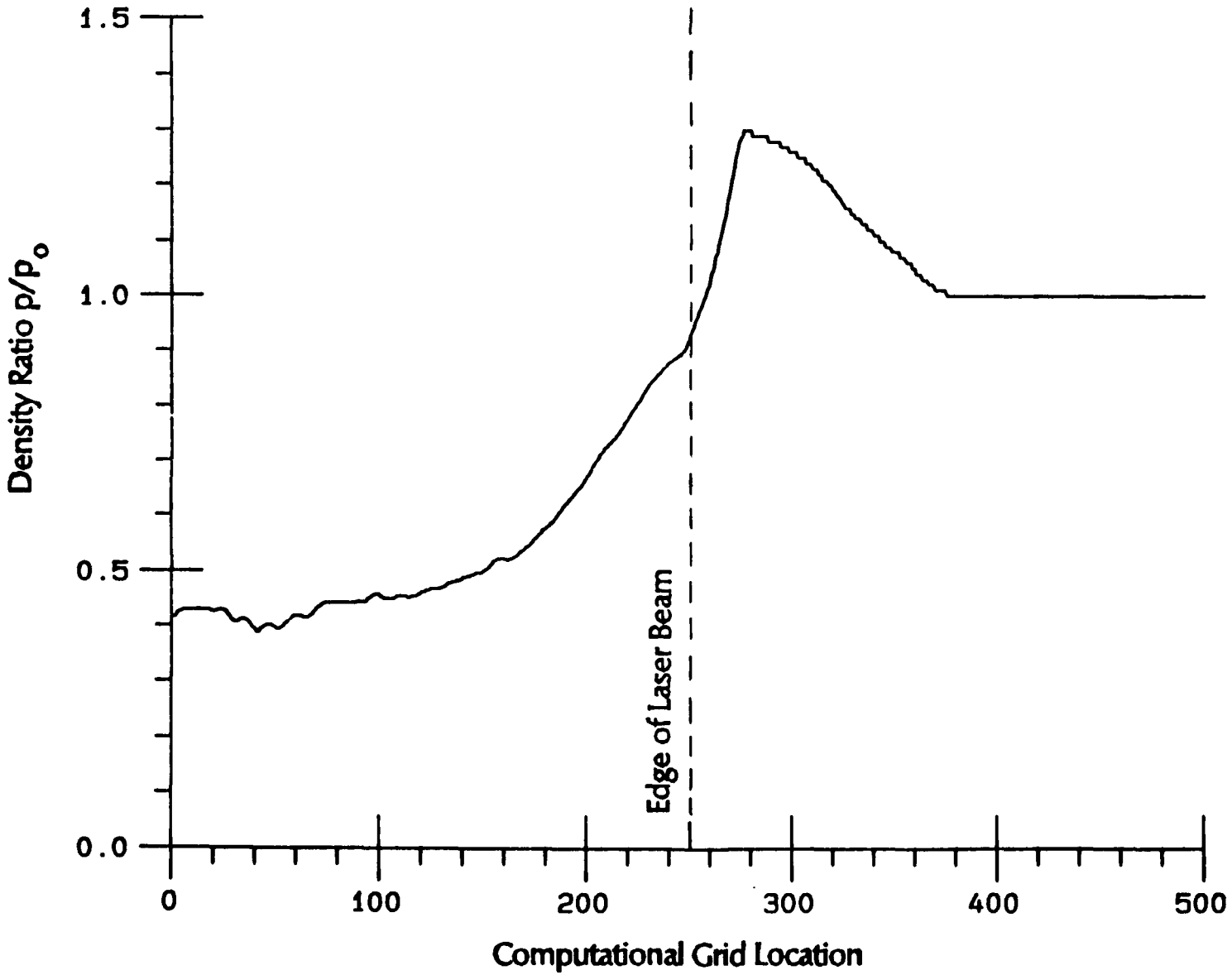

Figure 2. Density ratio calculated at 46 ns after pulse 8 in argon.

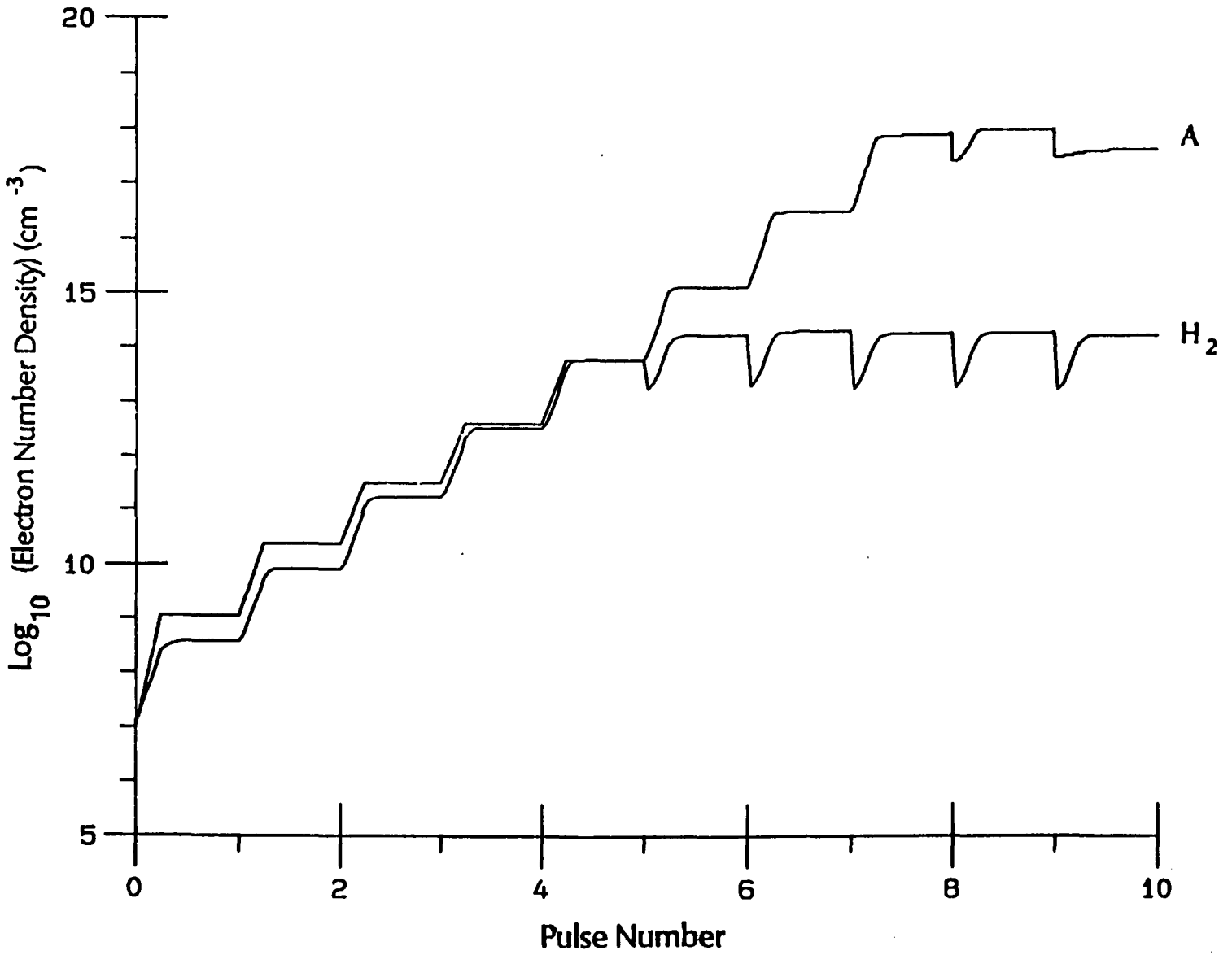

Figure 3. Electron density increase for a sequence of 10 laser pulses in argon and hydrogen at a pressure of 1 atmosphere.

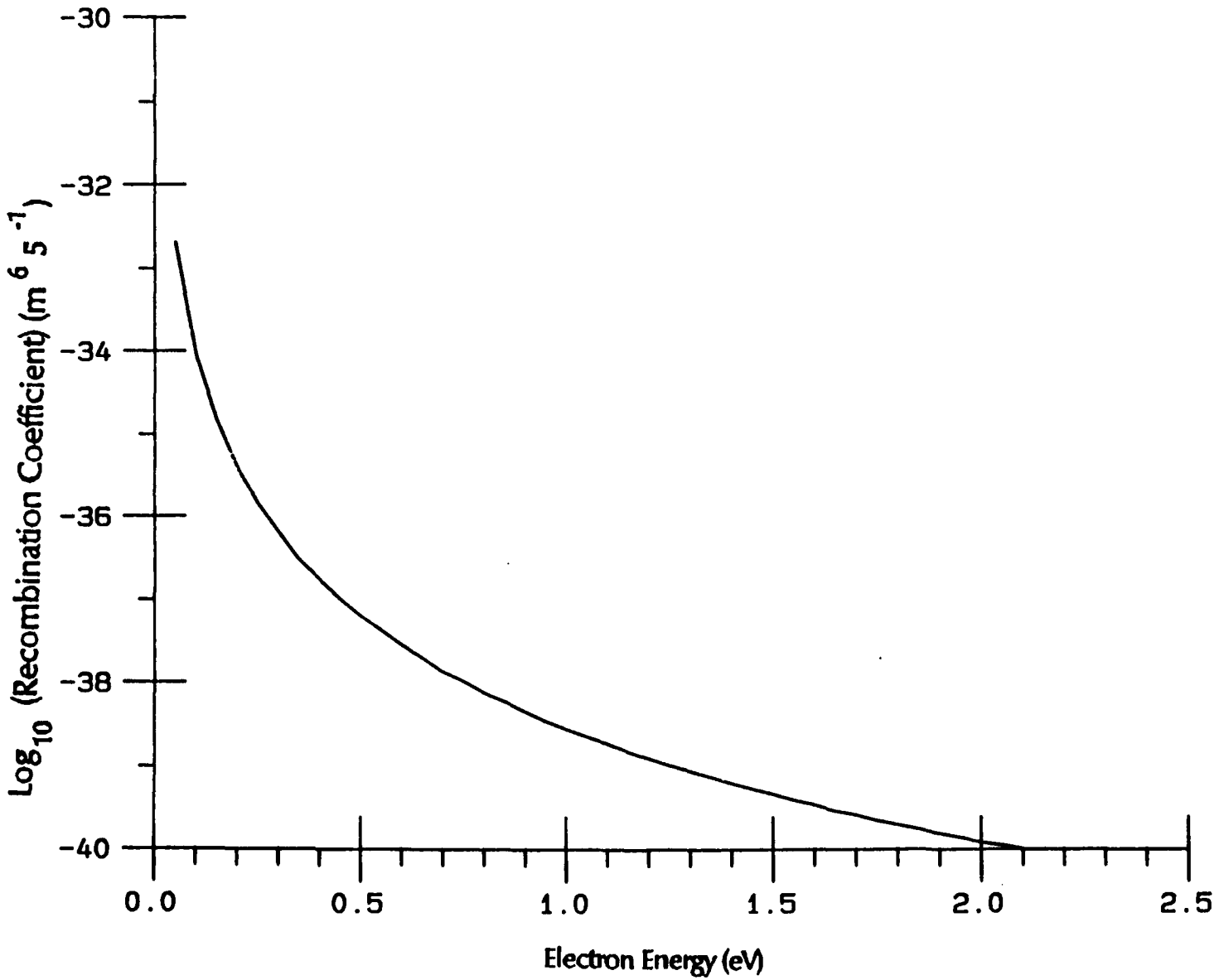

Figure 4. Three body recombination coefficient.

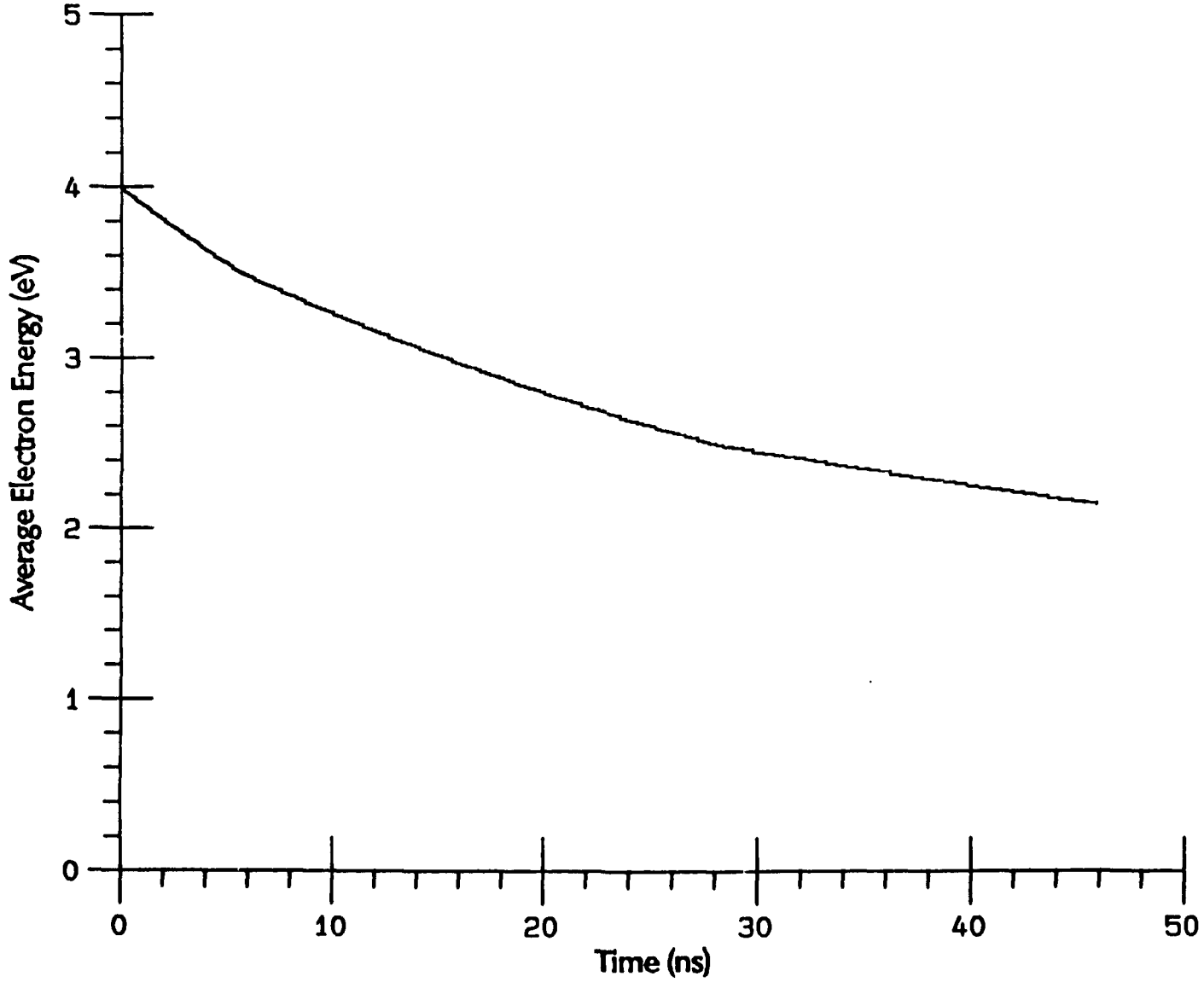

Figure 5. Relaxation of the electron energy in argon during the 46 ns interval between laser pulses.

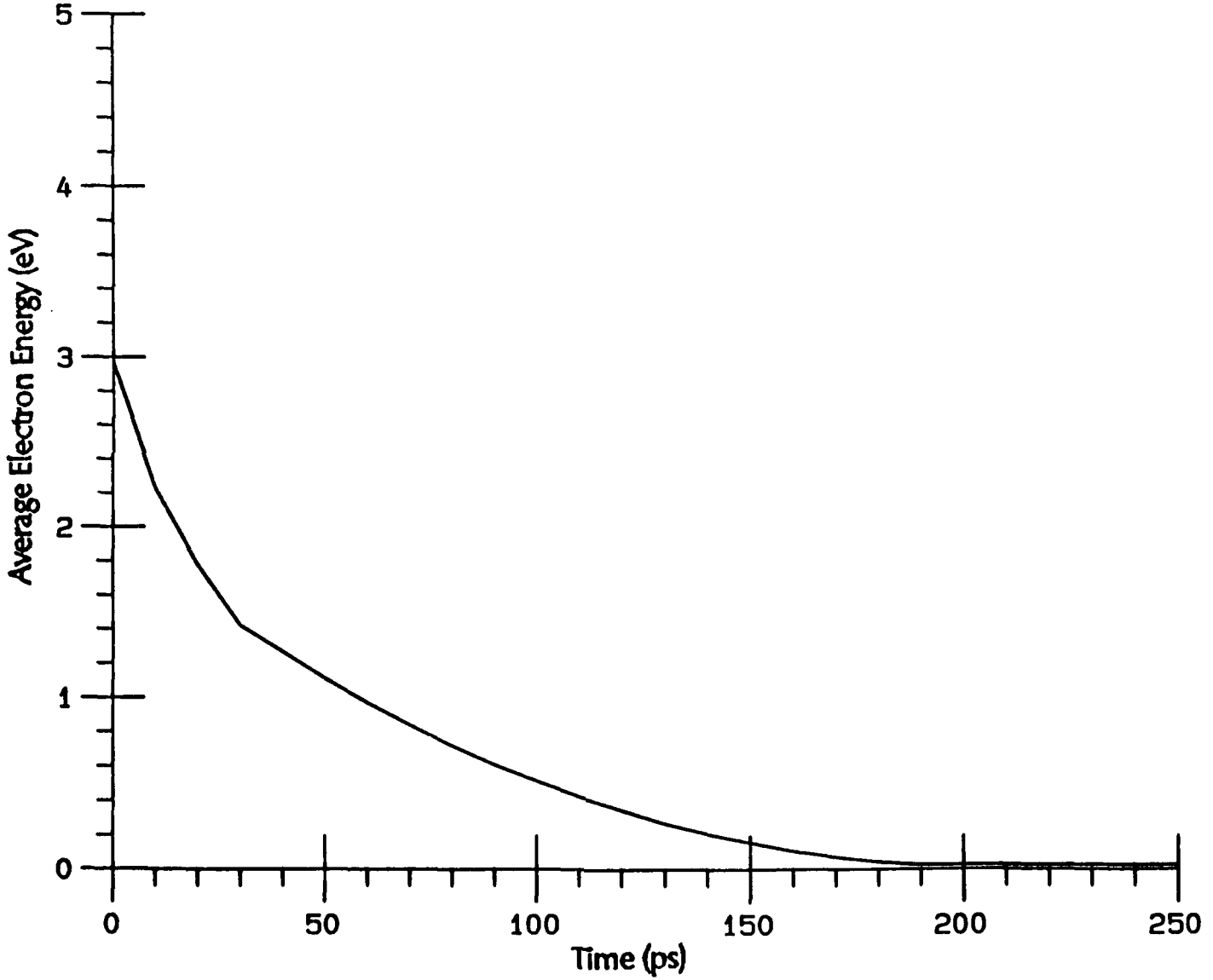

Figure 6. Relaxation of the electron energy in hydrogen during the 46 ns interval between laser pulses.

APPENDIX A

LASER PROPULSION USING FREE ELECTRON LASERS

Dennis Keefer,‡ Ahad Sedghinasab,† Newton Wright,* Quan Zhang**

Center for Laser Applications
University of Tennessee Space Institute
Tullahoma, TN 37388

Abstract

Quasi-steady plasmas have been initiated and sustained in argon at pressures from one to three atmospheres using power absorbed from a 10.6 micron wavelength laser beam produced by the RF linac free electron laser at Los Alamos National Laboratory. The pulse format of the RF linac laser consisted of an 80 microsecond long burst of 10 ps pulses separated by 46 ns, with an average power of approximately 3.75 kW. Time-resolved spectroscopic observations revealed no decay of the plasma during the 46 ns interpulse time. Analysis of the spectroscopic data using Boltzmann factors, ion-neutral intensity ratios and absolute emission coefficients gave values of the plasma temperature that varied from 17,500 K to 20,000 K during the 80 microsecond pulse. Attempts to obtain optical breakdown in nitrogen and hydrogen proved unsuccessful, even at optical intensities ten times the observed threshold for argon.

I. Introduction

In a propulsion system supported by a laser-sustained plasma (LSP), the high-power laser beam from a remote site is focused into the thruster. The plasma is ignited and continuously sustained near the laser focus. The plasma is used to absorb the power from the laser beam and convert it into propellant enthalpy.

---

‡ Professor of Engineering Science & Mechanics
Member AIAA
† Research Associate
* Engineer
** Graduate Research Assistant

Application of high power laser sustained plasmas (LSP) to space propulsion technology requires a fundamental understanding of the mechanisms by which a laser beam can initiate and sustain a plasma under various flow and power conditions. Interactions between the laser beam and the flowing plasma is complex and highly nonlinear, and detailed experiments have been required to gain a quantitative understanding of these processes.[1] A series of experimental investigations has been conducted at The University of Tennessee Space Institute (UTSI) using a 1.5 kW continuous (CW) CO_2 laser to obtain detailed measurement of the plasma temperature field in an argon LSP.[2] Laser power absorption and radiative emission were calculated from the measured temperature field to provide a detailed understanding of the energy conversion processes. Based on the experimental results, a detailed computational model was developed which provides a comprehensive description of the LSP in convective flow environments.[3] Similar work has been performed at The University of Illinois using a CW CO_2 laser at powers up to 10 kW and with a maximum flow velocity of 30 m/s at a pressure of one atmosphere.[4] Plasma absorption and thermal efficiencies using various gas mixtures and optical configurations were the main focus of these experiments. The computational code developed at UTSI was extended to provide a detailed design for a 30 kW laser powered thruster using hydrogen as a propellant.[5]

A comprehensive evaluation of laser-based propulsion systems has determined that lasers in the megawatt power range will be required to insure the practicality of this concept.[6] Presently, pulsed free electron lasers (FEL) appear to be the most promising way to provide these power levels. These lasers can provide both nanosecond and picosecond pulses, but the RF Linac laser may be able to provide a quasi-continuous beam consisting of trains of picosecond pulses. Optical plasma breakdown using pulsed CO_2 lasers has been studied for two decades, but these experiments were all conducted using essentially single laser pulses of nanosecond or longer duration. We conducted these experiments at Los Alamos National Laboratory (LANL) to evaluate the feasibility of using the RF Linac laser to sustain quasi-steady plasmas.

Prior to the experiments performed at LANL, the decay characteristics of argon optical

breakdown plasmas were studied at the Center for Laser Applications at The University of Tennessee Space Institute using a Lumonics XeCl excimer laser with wavelength of 308 nm and pulsewidth of approximately 20 ns. An optical multichannel analyzer (OMA) was used to record the radiation spectrum of the argon plasma created within a closed cell. Spectra were recorded in 10 ns steps with 10 ns gatewidth for up to 15 μs after the plasma initiation. These preliminary studies indicated that the decay rate of an argon optical breakdown plasma is of the order of microseconds, which is much longer than the interpulse time of the LANL laser, and suggested that it was feasible to sustain an argon plasma with the pulse format of the LANL RF Linac free electron laser.

In the following sections we describe the experimental facilities, experimental procedures, spectral data reduction, and plasma temperature determination using several spectroscopic techniques.

II. Experiment

A quasi-steady argon plasma was sustained by the LANL free electron laser in a flow chamber which was constructed with zinc selenide windows on both ends so that a direct measurement of laser absorption could be obtained. The flow tube, where the plasma was sustained, had a diameter of 1 cm to provide relatively high incident flow velocities at moderate mass flow rates. An annular flow was provided at the surface of the entrance window to provide cooling.

The RF linac free electron laser was tuned to a wavelength of 10.6 μm to provide direct comparison with the experiments performed using CO_2 lasers. The output beam of the FEL operated in a gaussian TEM_{00} mode with 80-120 μs macropulses which were repeated at a rate of 1 Hz. The macropulse energy was approximately 300 mJ, giving an average power of 3.75 kW during an 80 μs burst. Each 80 μs burst consists of approximately 1700 micropulses that have a duration of approximately 10 picoseconds and are spaced 46 nanoseconds apart to provide a peak power of about 17 MW. The laser output beam was focused into the flow chamber by a zinc selenide lens with focal length of 127 mm. The spot size was calculated to be about 95 microns in diameter resulting in a peak power

density of 10^{11} W/cm^2 for a 120 mJ macropulse.

A variety of diagnostic measurements were made during the experiment. A Hadland image converter camera was interfaced with a CID video camera to provide digital images that were acquired using a Matrox framegrabber housed in a Masscomp computer. This provided high-speed images of the transient plasma formation and decay at a framing rate of 100,000 frames per second. Time resolved spectra of the plasma were obtained using the OMA in a manner similar to that used for the excimer laser generated plasma. The OMA gatewidth was set to 10 ns and 10 spectra were accumulated from 10 successive macropulse breakdowns to average the results of several realizations of the plasma and to enhance the signal-to-noise ratio. The OMA was then delayed for 10, 20, 30, 40 and 50 ns, and the spectral data accumulation was repeated for each delay setting. Similar spectra were also obtained at 20 μs intervals throughout a 120 μs burst. The OMA was calibrated for absolute intensity using both tungsten ribbon and deuterium arc standard lamps. Wavelength calibration was obtained using mercury and argon spectral sources. A schematic of the experimental apparatus is shown in Figure 1.

Data were obtained for FEL sustained argon plasmas at pressures of 1 and 3 atmospheres over a range of incident flow velocities. These plasmas were easily initiated at all pressures, and nearly complete absorption of the incident laser beam was measured by the two energy meters installed upstream and downstream of the flow chamber.

Hydrogen and nitrogen gases were also introduced to the flow chamber, in separate experiments, in an attempt to study the differences in the initiation and plasma characteristics between these gases and argon. However, self initiation was never achieved in these molecular gases, even at ten times the power required for argon breakdown.

III. Spectral Data Reduction

The spectral data acquired by the OMA were calibrated for both wavelength and absolute intensity. Spatially calibrated framing camera images were used to determine the plasma shape and size. The contribution of the continuum radiation to the absolute values of the spectral lines of interest was subtracted by fitting a straight line to the

adjacent continua of that line. To determine the absolute intensity of the overlapping lines Lorentzian profiles were fitted to the lines, since Stark broadening is the dominant broadening mechanism for atmospheric pressure argon plasmas. The plasma was assumed to be optically thin, since the measured absolute emission coefficients described below yielded an optical thickness of about 6×10^{-3}.

Several different spectroscopic methods were used to calculate the argon plasma temperature from the plasma intensity measurements. The first method used the relative emission coefficient ratio of an argon ion line and a neutral line given by,[7]

$$\frac{I_i}{I_a} = 2\frac{\lambda_a A_i g_i}{\lambda_i A_a g_a}\left(\frac{2\pi m_e kT}{h^2}\right)^{3/2}\frac{1}{n_e}\exp\left(-\frac{E_i - E_a}{kT}\right) \tag{1}$$

where

$$I = \int_{\Delta\lambda} I(\lambda)d\lambda$$

The subscripts i and a refer to ion and neutral respectively. λ is the transition wavelength, $\Delta\lambda$ is the total width of the line at the continuum base, A is the transition probability, g is the statistical weight of the transition upper level, n_e is the electron density, E is the upper level energy relative to the ground state of the neutral atom, and k is the Boltzmann constant. This method requires a knowledge of the electron density. The electron density can be obtained by an iterative solution of the ideal gas law and the Saha equations at the measured pressure, with the assumption of two stages of ionization, quasi-neutrality, and local thermodynamic equilibrium (LTE);

$$p = (n_e + n_i + n_{ii} + n_a)kT \tag{2}$$

$$n_e = n_i + 2n_{ii} \tag{3}$$

$$\frac{n_e n_i}{n_a} = \frac{2Z_i}{Z_a}\left(\frac{2\pi m_e kT}{h^2}\right)^{3/2}\exp\left(-\frac{E_I}{kT}\right) \tag{4}$$

$$\frac{n_e n_{ii}}{n_i} = \frac{2Z_{ii}}{Z_i}\left(\frac{2\pi m_e kT}{h^2}\right)^{3/2}\exp\left(-\frac{E_{II}}{kT}\right) \tag{5}$$

Here subscript ii denotes the second stage of ionization, Z is the electronic partition function, E_I is the first ionization potential, E_{II} is the second ionization potential, and p denotes the chamber pressure.

The uncertainty in the resulting values of temperature based on the uncertainties of other parameters in Eq. (1) can be estimated as

$$\frac{\Delta T}{T} \simeq \left[\frac{\Delta(I_i/I_a)}{I_i/I_a} + \frac{\Delta(A_i/A_a)}{A_i/A_a} + \frac{\Delta n_e}{n_e}\right] \frac{kT}{E_i - E_a} \tag{6}$$

For $T = 20,000$ K, $(E_i - E_a)/KT \simeq 14$ for the spectral lines considered here. Therefore, even significant uncertainties in I_i/I_a or n_e, would only result in a small error in the temperature values.

In the second method, the relative upper level populations of argon ion lines are obtained from the relative intensity of the lines using

$$n_m = C\frac{\lambda_{mn}}{A_{mn}} I \tag{7}$$

where C is the proportionality constant. The logarithm of level population ratios are then plotted against the upper level energies. Boltzmann factors given by,

$$\log\left(\frac{n_m/g_m}{n_n/g_n}\right) = -\frac{1}{T}\left(\frac{E_m - E_n}{k}\right) \tag{8}$$

is then used to determine the plasma temperature from the slope of a straight line which is least squares fitted to all the points on the plot. This method assumes that the upper level densities of all the measured lines are distributed according to a single equilibrium temperature. The accuracy of this method depends both on the number of spectral lines used and differences in their energy levels.

In the third method the temperature was calculated from the line emission coefficient which was determined from the measured absolute line intensity, $\mathrm{I_{abs}}$, using,

$$\epsilon_L = \frac{\mathrm{I_{abs}}}{\ell} \tag{9}$$

where ℓ is the length of the plasma in the direction of line of sight. The value of ℓ was obtained from the framing camera images. The upper level populations of the ionic lines are then calculated from

$$n_m = \frac{4\pi\lambda_{mn}\epsilon_L}{hcA_{mn}} \tag{10}$$

The ionic ground state density is related to the upper level densities by the Boltzmann factor,

$$\frac{n_m}{n_i} = \frac{g_m}{Z_i} \exp\left(-\frac{E_m}{kT}\right) \tag{11}$$

If we assume that the plasma is in LTE, then Equations (2-5) and Equation 11 can be solved simultaneously to yield plasma temperature and composition.

In each of the methods described above, spatially averaged intensity data were used to calculate the plasma temperature. Since the relative intensities were utilized in the first two methods, the error introduced by intensity averaging is minimal. However, in the third method, where absolute intensities were used, the use of spatially averaged intensities may introduce a more significant source of error. On the other hand, the intensity and temperature profiles of LSP's are relatively flat over most of the plasma, except for a small region near the boundaries, and the temperatures calculated using this technique are expected to be reasonable representations for the central portion of the plasma.

IV. Results

Quasi-steady argon plasmas were routinely self-initiated and sustained using the LANL free electron laser pulse format. Figure 2 shows the argon spectra taken each 10 ns for a total of 60 ns to insure the inclusion of at least one micropulse. This figure shows no significant difference between the spectrum which included the 10 ps pulse and those spectra taken during the 46 ns interpulse time. This result probably reflects the fact that the micropulse from the laser is "on" only 1/1000 of the total 10 ns gate time of the OMA. Because of this low duty cycle, any unique spectral feature characteristic of the micropulse absorption would have little contrast relative to the background spectrum. In fact, the background spectrum exhibits no measurable change over the 46 ns interpulse time, indicating that the relaxation processes of the plasma are considerably longer than the interpulse time. This is to be expected, since most of the spectral lines in the recorded spectral range have transition times of the order of 100 nanoseconds. The only lines in ionic argon which have transition times of a few nanoseconds are the resonance lines, which were not recorded during these experiments. The argon plasma spectra recorded at 20 mi-

crosecond intervals during one macropulse is shown in Figure 3. The lowest line in this figure corresponds to the signal taken at 100 μs, at which time, the plasma has expanded and decayed more noticeably.

Plasma temperatures calculated using the ion-neutral line ratio method are presented in Figure 4. In this method, the relative emission coefficients of ion lines 3729, 3765, 3780, 3850, 3868, 3928, 4013, 4072, and 4103 Å were compared to those of argon neutral lines 4158 Å and 4200 Å. The plasma temperature is plotted versus time during one macropulse. The bars on each data point indicate the standard deviation of the temperature as determined from each of the 18 ion-neutral line pairs evaluated for the six sets of spectral data recorded at the 10 ns intervals. This scatter can be attributed to the errors involved in the deconvolution of the overlapping spectral lines, the assumption of plasma homogeneity, and the more basic uncertainties of the transition probability values.

Figure 5 shows a typical Boltzmann plot where the relative populations of various ionic excited levels are plotted versus the excited level energies. The slope of the fitted straight line is inversely proportional to the plasma temperature. The scatter in Figure 5 is primarily associated with the process of deconvolving the overlapping lines using fitted Lorentz profiles and straight line subtraction of the continuum. Transition probability uncertainties do not play an important role in the extent of the scatter in this case, since the relative values of the transition probabilities are usually accurate to within 5% for a single ionic species.[8] Plasma temperatures obtained by this method are shown in Figure 6.

In the last technique where the temperature has been determined from absolute line emission, the characteristic dimension of the plasma along the line-of-sight was obtained from the framing camera images, one of which is shown in Figure 7. The calculated plasma temperature (Figure 8) using this technique is fairly insensitive to the value used for the plasma size. A 50% error in the plasma diameter results in only a 4% change in the value of the calculated temperature for this particular temperature range. The bars on the temperature values represent one standard deviation resulting from the use of 9 different ion lines. As noted in Figures 4, 6, and 8, the plasma temperature decreased with time,

due to the expansion of the plasma about the focal region.

Although argon plasmas were easily self-initiated and sustained using the LANL free electron laser, we were unable to obtain optical breakdown in either nitrogen or hydrogen. In a laser sustained plasma at a wavelength of 10.6 μm, the dominant process of laser absorption is inverse bremsstrahlung, in which the electrons are accelerated in the strong electric field (10^9 V/m in this case) created by the laser, and subsequently undergo elastic, inelastic and ionizing collisions with neutral atoms. However, prior to breakdown there are few electrons available in the cold gas, and the electron neutral collision frequency is approximately 1 per picosecond. Therefore, it is likely that breakdown does not occur within the first micropulse but cascades to breakdown after several micropulses. Since the rate of optical energy absorption and the ionization potential are similar for the various gases used in our experiments, it is likely that the electron loss processes which take place during the 46 ns interpulse time is responsible for the observed differences in breakdown threshold. These loss processes include excitation of internal energy states of the molecular species, electron diffusion and, in the later phases of the breakdown cascade, gasdynamic expansion. Each of these processes proceed at considerably different rates for argon and the molecular gases, and are likely to be responsible for our failure to observe optical breakdown in hydrogen and nitrogen.

A detailed comparison of various features of FEL sustained plasmas to those of CO_2 laser sustained plasmas is not possible at this time due to the preliminary nature of the experiment. In this work parameters such as flowrate, optical depth of field, and pressure were not studied to their full extent. However, it is possible to conclude that argon plasmas were sustained by FEL which has a vastly different pulse format. The absorption of the laser energy by the plasma as measured by the Joule power meters were comparable to those encountered in CW CO_2 experiments ($80 - 90\%$).

V. Conclusions

The principal conclusions that can be drawn from these initial experiments are:

1. Argon plasmas are easily self-initiated and sustained by the LANL free electron laser

operating at 10.6 micrometers with 10 ps micropulses.

2. Spectral data taken with 10 ns gate times at 10 ns intervals did not reveal any changes in plasma radiation during the 46 ns interpulse time.
3. The various spectroscopic techniques used to calculate the plasma temperatures yielded temperature of 17,500 K to 20,000 K depending on the time during a macropulse.
4. Argon plasmas self-ignited at a power density of 10^{11} W/cm^2, but hydrogen and nitrogen did not undergo optical breakdown for power densities up to 10^{12} W/cm^2.

This experiment demonstrated the feasibility of using pulsed free electron lasers to ignite and sustain plasmas in a forced convection environment that could be used for space propulsion. Further experimental and theoretical research should be focused on the mechanisms responsible for the observed differences between picosecond optical breakdown thresholds in argon and the molecular gases.

Acknowledgement

The authors wish to thank Drs. Larry Warner, Jon Sollid, Dodge Warren and the entire crew at the FEL facility at Los Alamos National Laboratory for their expert and enthusiastic support during our experiments there. This work was supported by The Air Force Office of Scientific Research under Grant AFOSR-86-0317.

References

1. Keefer, D. R., "Laser Sustained Plasmas," Chapter 4, *Laser-Induced Plasmas and Applications*, edited by Leon J. Radziemski and David A. Cremers, Marcel Dekker, Inc., 1989, pp. 169-206.
2. Welle, R., Keefer, D., and Peters, C., "Power Absorption in Laser-Sustained Argon Plasmas, Part I," *AIAA Journal*, Vol. 24, No. 10, 1986, p. 1663.
3. Jeng, S. M., Keefer, D. R., Welle, R., and Peters, C. E., "Laser-Sustained Plasmas in Forced Convective Argon Flow, Part II: Comparison of Numerical Method with Experiment," *AIAA Journal*, Vol. 25, Sept. 1987, pp. 1224-1230.

4. Krier, H., Mazumder, J., Zerkle, D. K., Schwartz, S., Mertogul, A., "Laser Sustained Argon Plasma for Thermal Rocket Propulsion," *Journal of Propulsion and Power*, Vol. 6, No. 1, Jan.-Feb. 1990, pp. 38-45.

5. Jeng, S. M. and Keefer, D., "Theoretical Evaluation of Laser-Sustained Plasma Thruster Performance," *AIAA Journal*, Vol. 5, No. 5, Sept.-Oct. 1989, pp. 577-581.

6. Kantrowitz, A., "Laser Propulsion to Earth Orbit - Has Its Time Come?," in: "Visions of Tomorrow; A Focus on National Space Transportation issues," *Proceedings of the Twenty-fifth Goddard Memorial Symposium*, Greenbelt, MD, March 18-20, 1987.

7. Venugopalan, M., "Reactions Under Plasma Conditions," Vol. 1, Wiley Interscience, New York, 1971, p. 396.

8. Sedghinasab, A., "Experimental Determination of Argon Atomic Transition Probabilities Using Non-LTE Diagnostics," Ph.D. Thesis, Georgia Institute of Technology, December 1987.

Figure 1. Schematic of the Experimental Diagnostic Configuration.

Figure 2. Argon plasma spectra obtained using 10 ns exposures. Six spectra were obtained at 10 ns intervals to include at least one micropulse, and all six spectra are superimposed in the plot.

Figure 3. Argon plasma spectra obtained using 10 ns exposures. Five spectra were obtained at 20 μs intervals, and all five spectra are superimposed in the plot.

Figure 4. Plasma temperatures obtained using the ion to neutral line ratio.

Figure 5. Typical Boltzmann plot for the argon ion lines.

Figure 6. Plasma temperatures obtained using the Boltzmann factors.

Figure 7. Images of the plasma formation and decay obtained at 100,000 frames per second. The laser direction is from bottom to top.

Figure 8. Plasma temperatures obtained using absolute line emission.

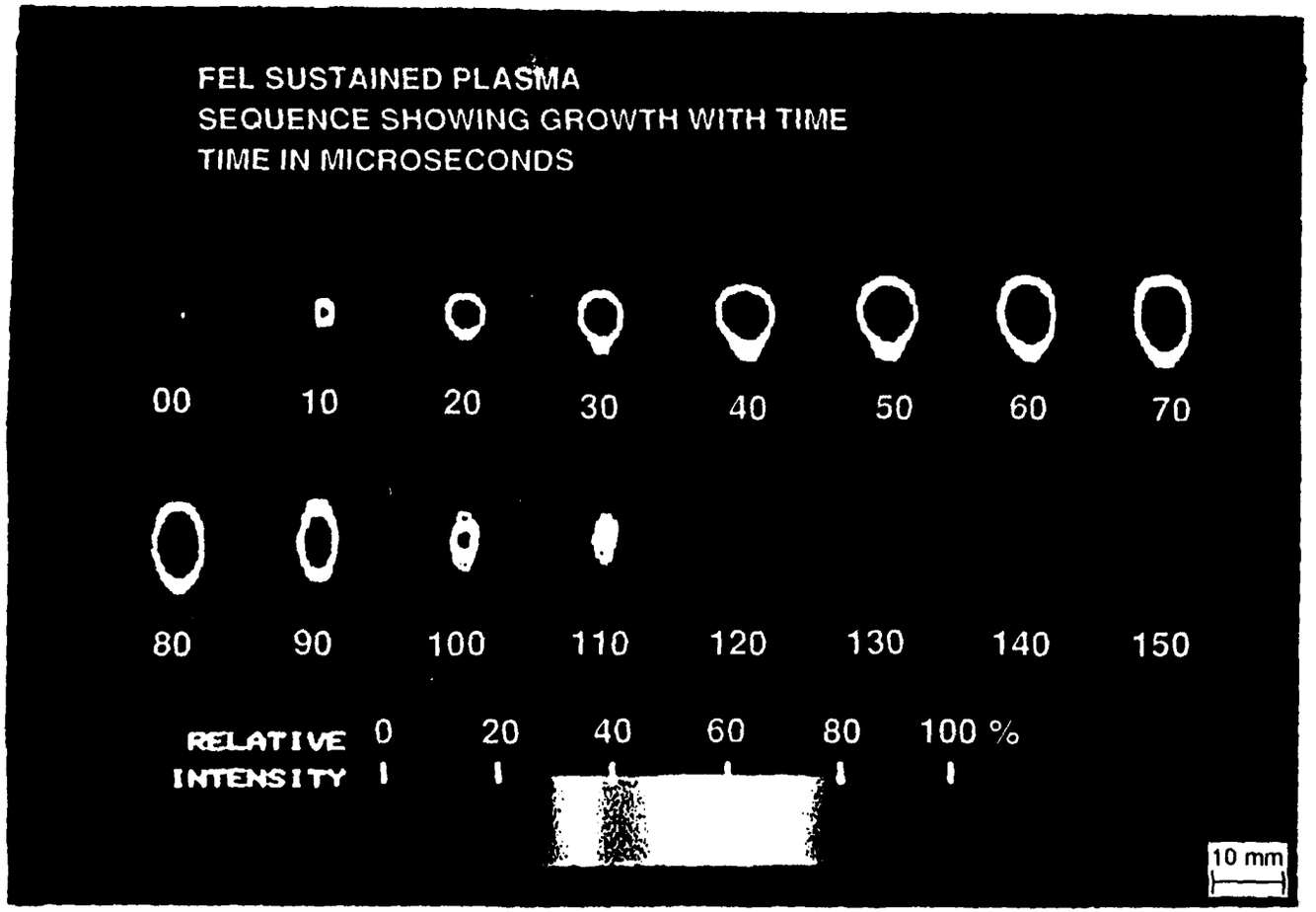
FEL SUSTAINED PLASMA
SEQUENCE SHOWING GROWTH WITH TIME
TIME IN MICROSECONDS
00
10
20
30
40
50
60
70
80
90
100
110
120
130
140
150
RELATIVE INTENSITY
0
20
40
60
80
100 %
10 mm

GL-3009

Fig. 7

BS Beam Splitter
JM Joule Powermeter
L Lens
OMA Optical Multichannel Analyzer

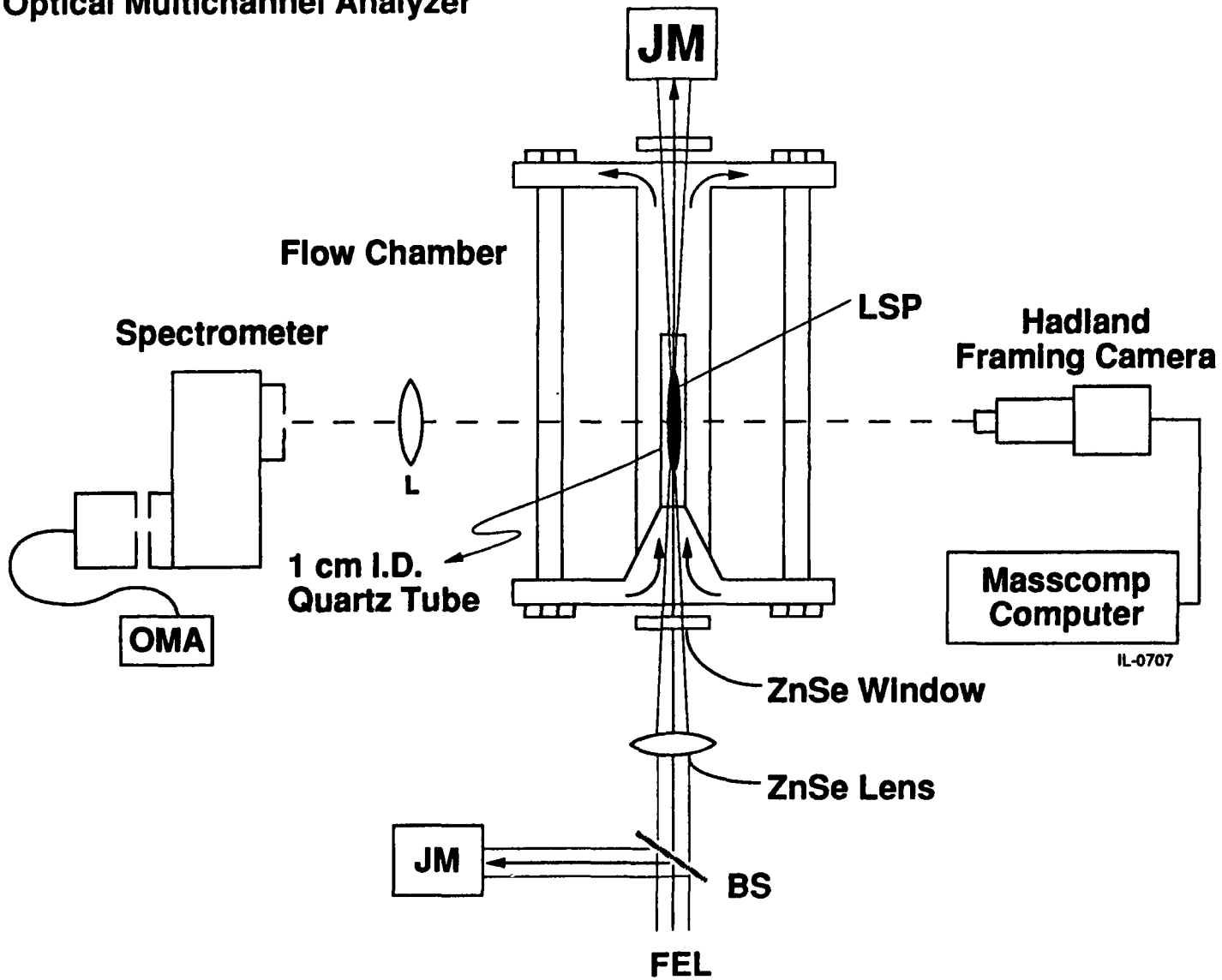

Fig. 7

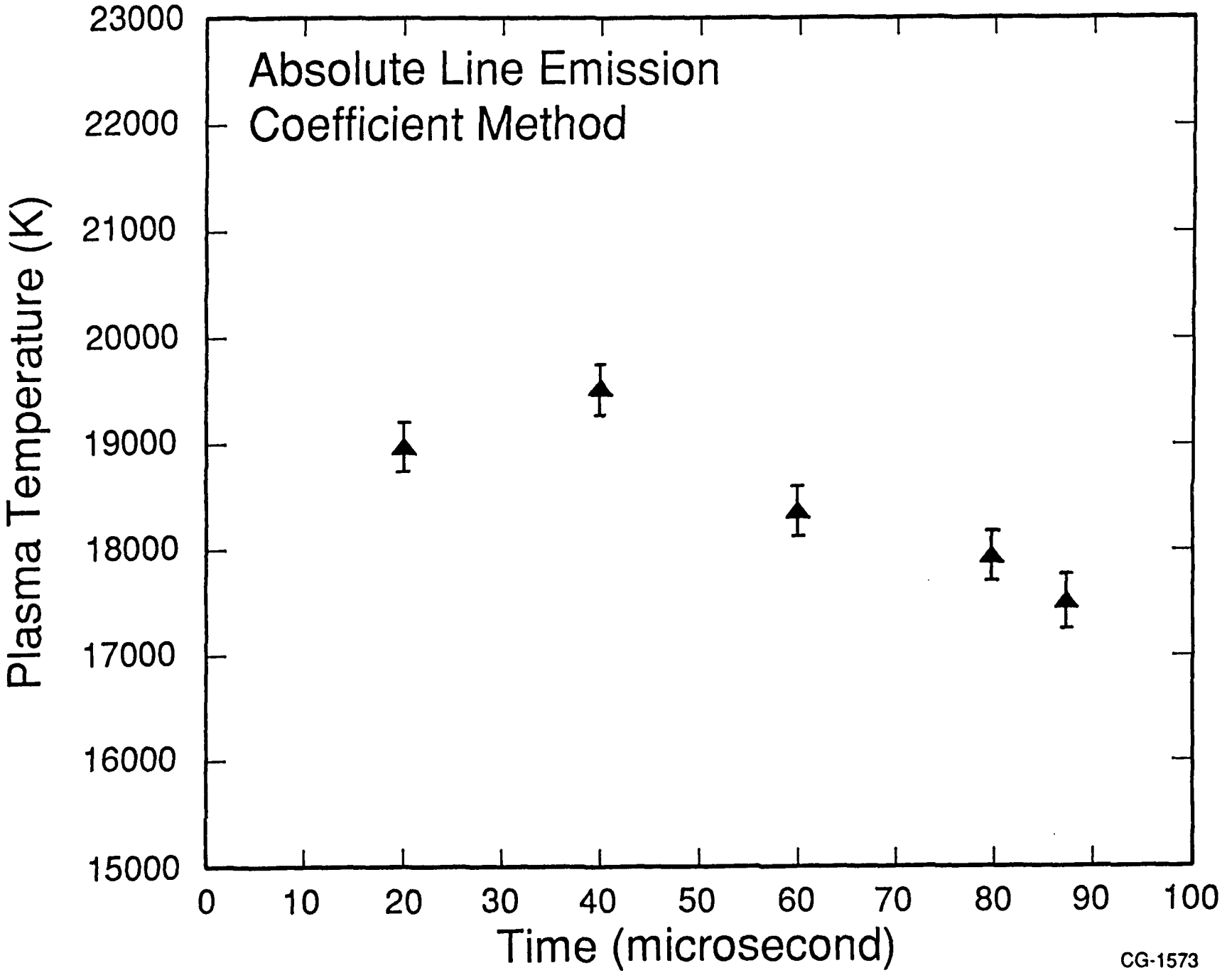
Absolute Line Emission
Coefficient Method
Plasma Temperature (K)
23000
22000
21000
20000
19000
18000
17000
16000
15000
0
10
20
30
40
50
60
70
80
90
100
Time (microsecond)
CG-1573

Fig. 8

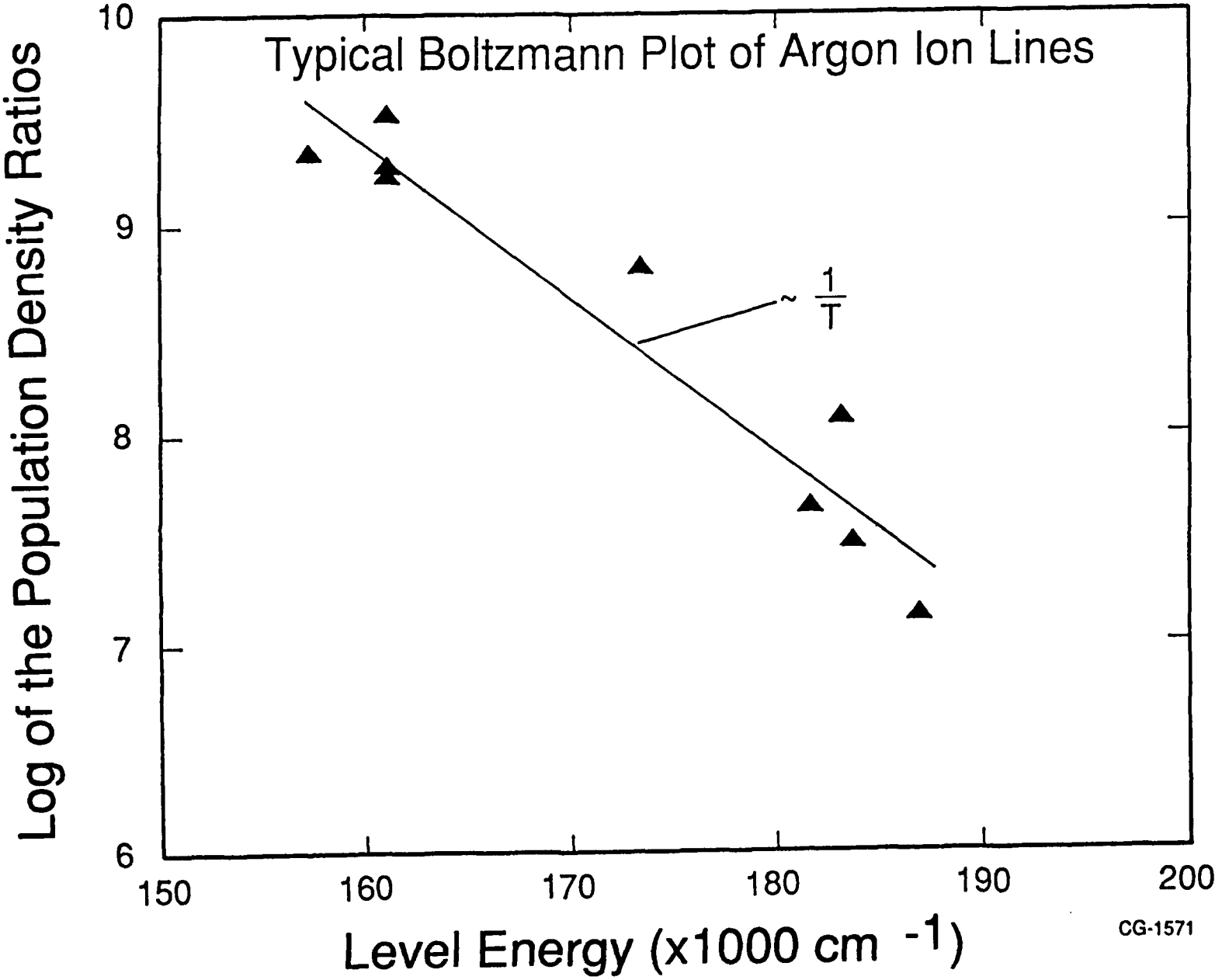
Typical Boltzmann Plot of Argon Ion Lines
Log of the Population Density Ratios
10
9
8
7
6
150
160
170
180
190
200
Level Energy (x1000 cm -1)
~ 1/T
CG-1571

Fig. 5

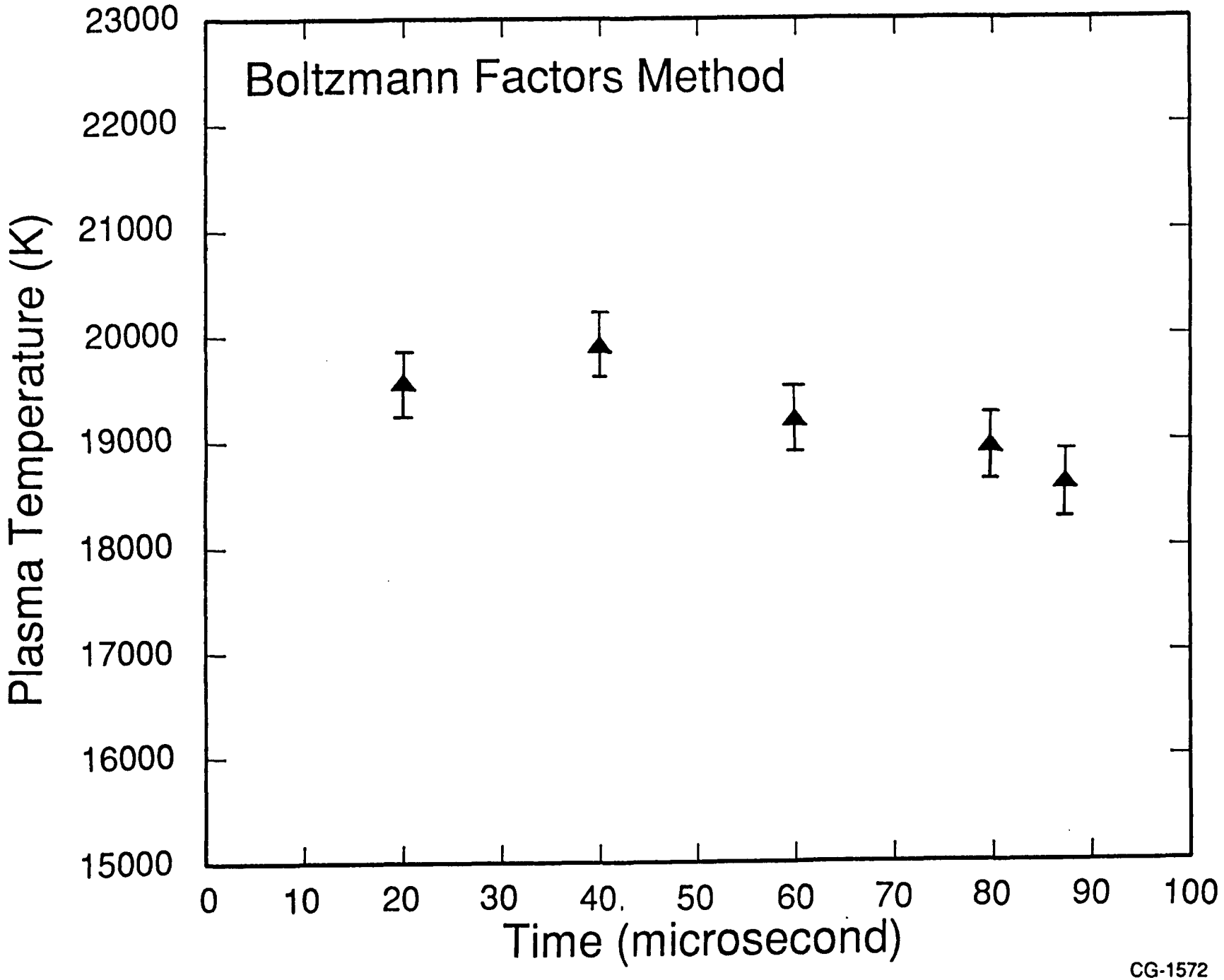
Boltzmann Factors Method
Plasma Temperature (K)
23000
22000
21000
20000
19000
18000
17000
16000
15000
0
10
20
30
40
50
60
70
80
90
100
Time (microsecond)
CG-1572

Fig. 9

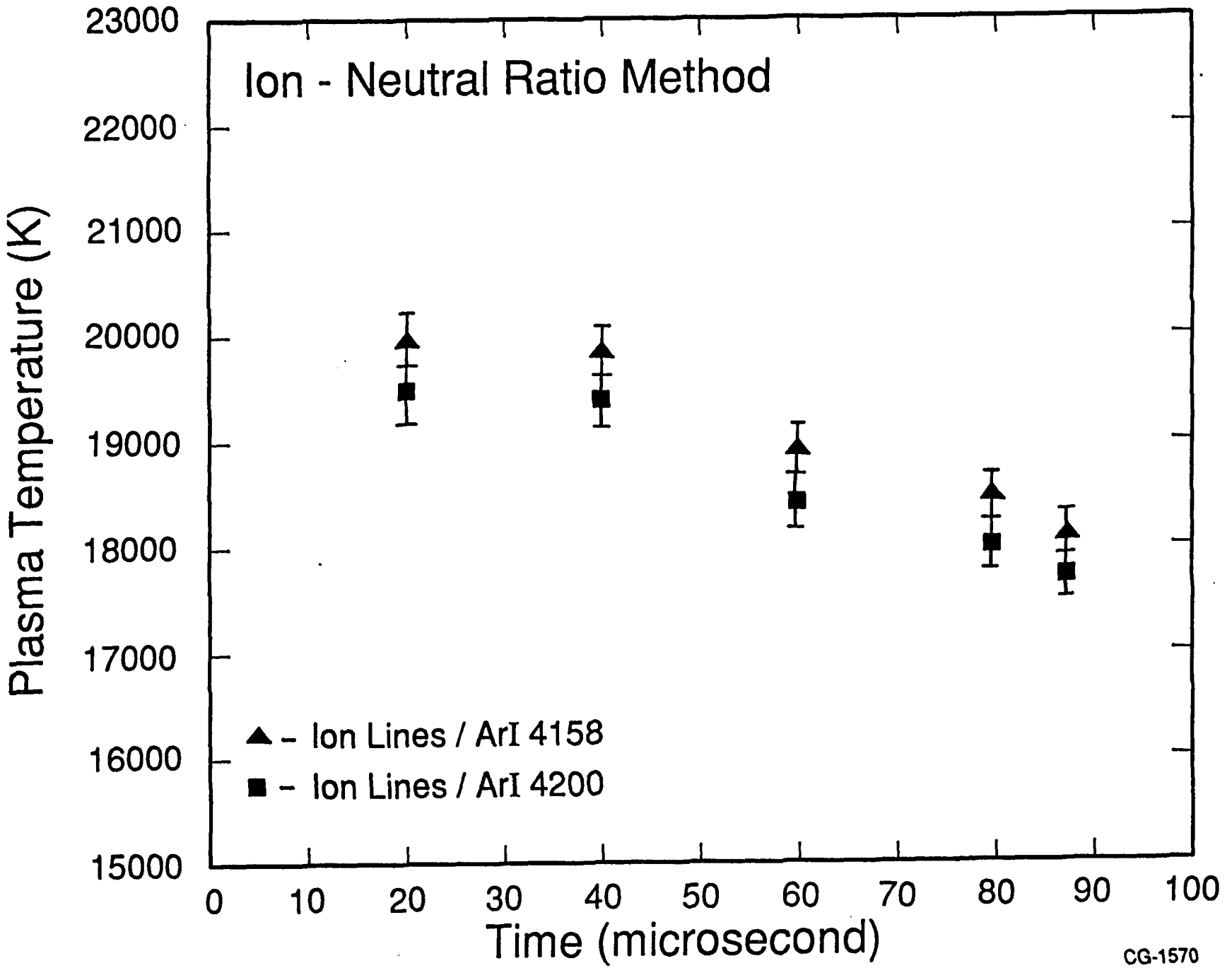
Ion - Neutral Ratio Method
Plasma Temperature (K)
23000
22000
21000
20000
19000
18000
17000
16000
15000
0
10
20
30
40
50
60
70
80
90
100
Time (microsecond)
▲ - Ion Lines / ArI 4158
■ - Ion Lines / ArI 4200
CG-1570

Fig. 4

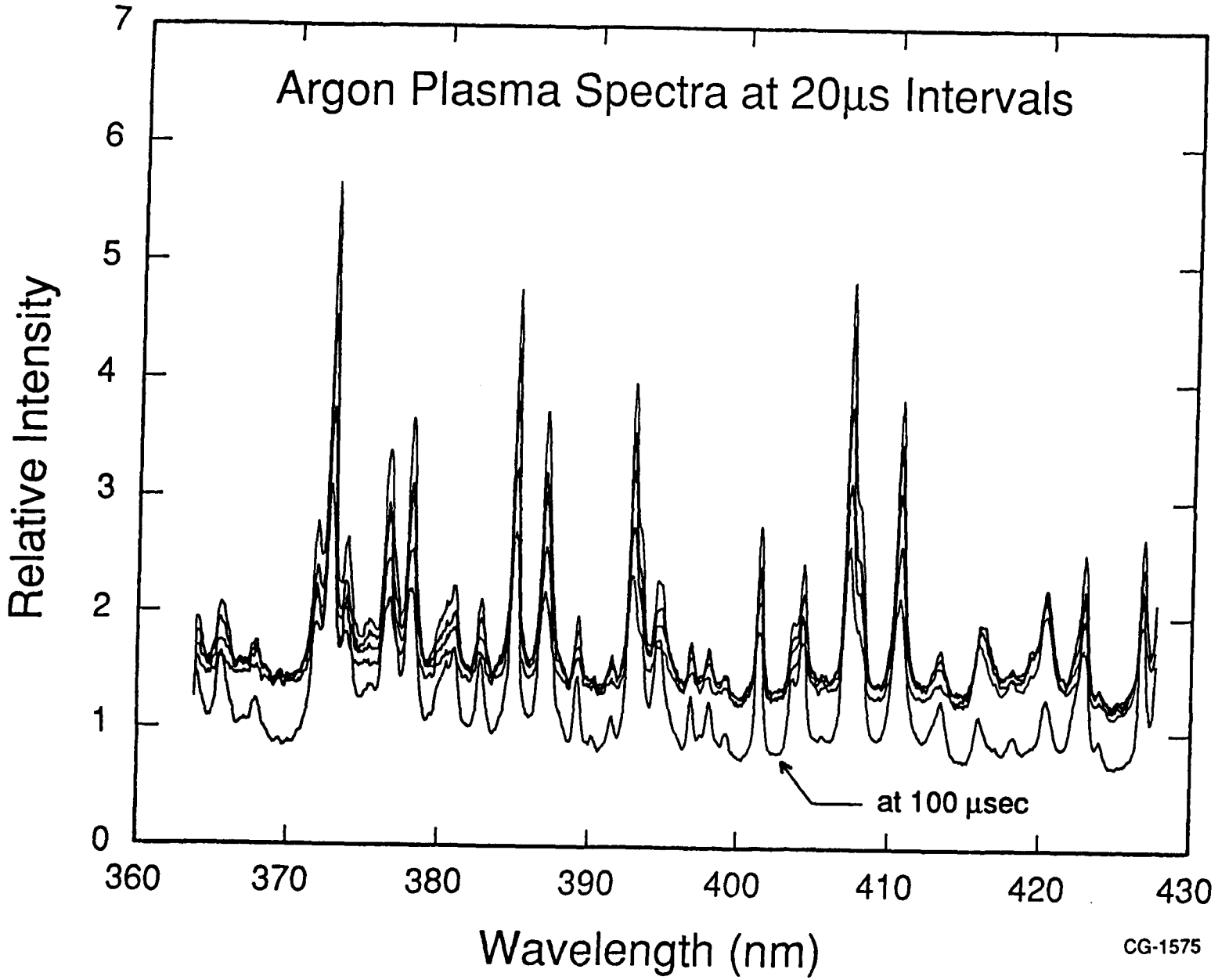
Argon Plasma Spectra at 20µs Intervals
Relative Intensity
0
1
2
3
4
5
6
7
360
370
380
390
400
410
420
430
Wavelength (nm)
at 100 µsec
CG-1575

Fig. 3

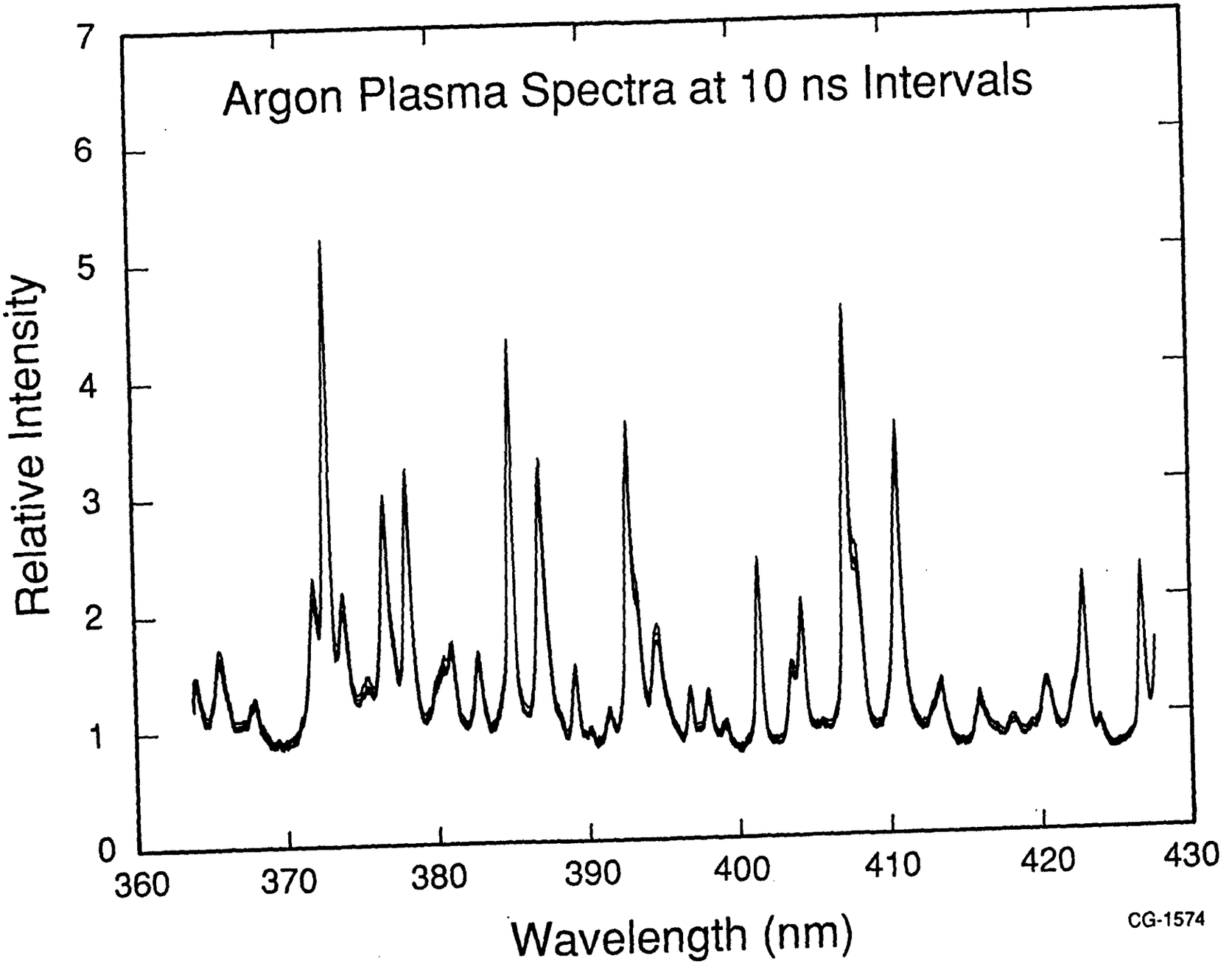
Argon Plasma Spectra at 10 ns Intervals
Relative Intensity
0
1
2
3
4
5
6
7
360
370
380
390
400
410
420
430
Wavelength (nm)
CG-1574

Fig. 2

APPENDIX B

Picosecond Resolved Evolution of Laser Breakdown in Gases

Lloyd M. Davis, Li-Qiang Li and Dennis R. Keefer

Center for Laser Applications,
University of Tennessee Space Institute, Tullahoma, TN 37388
Ph. (615) 455-0631

ABSTRACT

Subpicosecond pulses from a synchronously-pumped dye laser were used to collinearly probe the absorption of laser breakdown plasmas formed by focusing longer (60 *ps* FWHM) 532 *nm* pulses from a regenerative amplifier into a cell containing helium, argon or nitrogen. The absolute time delay between the 532 *nm* pulses and the probe pulses was varied in order to measure the initiation time and the rate of growth of the plasma for different pressures and breakdown pulse energies. In general, at the higher pressures for which cascade ionization processes are expected to dominate, the onset of the plasma is found to be quite abrupt compared to the duration of the breakdown pulse. The initiation time is earlier and the rate of growth is faster if the breakdown pulse energy or pressure is increased. For argon and nitrogen at lower pressures, slow growth of the plasma can continue for hundreds of picoseconds after the breakdown pulse has passed, indicating that relaxation from a nonequilibrium state occurs.

I. Introduction

Breakdown at the focus of a pulsed laser beam has been observed since the advent of the Ruby laser nearly 30 years ago[1,2] and a considerable body of literature aimed at understanding the physical mechanisms for optical breakdown in transparent media has since developed.[3] Breakdown in gases can be caused by direct ionization or, when the pressure is sufficiently high, by cascade or avalanche growth of ionization due to inverse Bremsstrahlung absorption of energy by free electrons followed by collisional ionization.[4] Direct ionization is generally due to multiphoton absorption[5,6] but at longer laser wavelengths where a larger number of photons would be needed, or at large laser intensities, it may be due to the tunneling of the electrons in the presence of the strong laser field.[7] Photo-ionization of excited intermediate atomic or molecular states is also important for certain gases.[8]

To date, experiments have centered largely on the measurement of the breakdown threshold for various conditions.[9--13] "Breakdown" is usually defined by the optical detection of the luminous plasma emission or the acoustical detection of the shock wave.

For longer, nanosecond laser pulse lengths, the threshold is generally found to be inversely dependent on the pulse length and on the pressure indicating that a collisional mechanism for the onset of breakdown is predominant. For shorter laser pulses ($\leq$ 10 *ps*) or low pressures, the breakdown threshold is considerably higher and only weakly dependent on pressure indicating that direct ionization by the laser pulse is the predominant mechanism.

It is well recognized that the various mechanisms may act simultaneously and that their relative contributions not only depend on the initial conditions but also change during the growth of the plasma. Indeed, theoretical modelling of the laser induced breakdown has developed to quite a sophisticated level[12,14] and may include all these effects and predict the growth of the plasma with time, but the point of comparison with experiment is generally the dependence of the breakdown threshold on the initial conditions of gas, pressure, laser wavelength and intensity. In some experiments, aspects of the breakdown process have been followed with nanosecond resolution.[15--18] Ireland *et al.* have published

Schlieren images of a laser plasma $\sim$ 20 ps following breakdown.[19]

In order to gain better understanding of the role of the various mechanisms at different stages of breakdown, we have conducted pump and probe experiments which permit the growth of a plasma to be followed with a time resolution of a few picoseconds. In addition, we have monitored the relaxation time of the plasma by measuring the absorption of probe pulses which pass many nanoseconds after the plasma is formed.

II. Experimental Apparatus

The experimental setup, as shown in Figure 1, consists of a standard collinear 'pump and probe' configuration, with the pump pulses originating from a Nd:YAG regenerative amplifier (Continuum RGA-60-50) and the probe pulses being supplied by a synchronously-pumped hybrid-modelocked dye laser (Coherent 702-1). Thus the laser-breakdown plasma is formed by the 532 nm pulses from the regenerative amplifier, while the subpicosecond pulses from the dye laser are used to probe the absorption of the plasma versus temporal delay.

The dye laser produces pulses tunable from 565 nm to 610 nm at a repetition rate of 76 MHz, each with a pulse energy of about 2 nJ and with a width of about 0.7 ps, as determined by a background-free autocorrelator. The regenerative amplifier produces pulses at a repetition rate of 50 Hz with a pulse energy of about 40 mJ at 1064 nm and with a width of about 90 ps. These pulses pass through a variable attenuator consisting of a rotatable half-wave plate and dichroic polarizer before being frequency doubled in a KDP crystal to yield 532 nm pulses with energies of up to about 12 mJ. Because both the regenerative amplifier and the synchronously-pumped dye laser are pumped by the same acousto-optically mode-locked Nd:YAG oscillator (Coherent Antares 76-s), the pulse trains have a well defined timing with respect to each other, even though they have considerably different repetition rates.

The 532 nm beam from the regenerative amplifier is collinearly combined with the dye laser beam using an uncoated quartz substrate which acts as a 10 % : 90 % beam splitter at 45 °. The peak intensity of the probe pulses is five orders of magnitude less than that of the breakdown pulses. Both beams are vertically polarized at the quartz substrate.

The portion of 532 nm beam which is split from the first interface of the quartz

substrate falls upon a piece of frosted glass and the light transmitted by this is passed through a calibrated neutral density filter (ND 2.02) to a photodiode in order to monitor the pulse energy and pulse-to-pulse fluctuations. (The portion of dye laser beam from this interface is simply removed by an aperture as shown in Figure 1.) Thus approximately 80 % of the 532 nm pulses and 10 % of the dye laser beam from the second interface of the quartz substrate pass through the aperture and are focused into the sample cell by a plano-convex lens with focal length of 7.84 cm. The diameter of the beams at the lens is approximately 0.46 cm resulting in an effective f-number of $f/17$.

The beam divergence of the dye laser beam at the focusing lens is adjusted so that it focuses at the same position as the 532 nm beam, by passing it through a pair of lenses with adjustable separation. This is conveniently accomplished by removing the sample cell except for the first window, locating the focal plane of the 532 nm beam by observation of the speckle pattern of largest grain in the back-reflected light from a razor blade as it is translated through the focus, and then adjusting the separation of the pair of lenses so that the back-reflected dye laser light also has largest speckle grain. At this time, the waist of 532 nm beam is measured by monitoring the ratio of transmitted pulse energy as the razor edge is transversely translated by a stepping motor. The transmission ratio versus razor position is well fitted by a Gaussian error function, yielding a beam waist of $7.8 \pm .2\ \mu m$.

Also at this time, the 532 nm pulse energy monitor photodiode is calibrated so that the pulse energy available for forming a plasma can be known from the energy monitor photodiode voltage. A pulse energy probe (Lasermetrics RJ-7200/RJP-734) is placed immediately after the first window of the sample cell, well before the focus position. To avoid damaging the probe, the attenuator in the regenerative amplifier beam is adjusted in order to give a pulse energy of only about 1 mJ at the probe and the ND 2.02 neutral density filter is removed from the monitor photodiode. The pulse energy at the probe is recorded on a personal computer using a locally constructed BCD/RS232 interface, while the photodiode voltage is captured on a boxcar integrator and transferred to the PC via GPIB. The photodiode is an HP2-4203 with locally constructed circuit and 20.0 volt battery supply and gives a pulse width of about 0.5 ns. Without the neutral density filter,

the pulse energy calibration factor is $1.24 \times 10^{-3}\ JV^{-1}$ over a range of pulse energies from 0.12 to 1.2 mJ. The pulse-to-pulse intensity fluctuations are about 5–10 %.

Following these initial calibration measurements, the sample cell is installed. The cell consists of a machined aluminum block, 5 cm × 6.3 cm × 10 cm long, with 1 inch uncoated quartz substrate windows at each end and a third window on the side for visual observation of the plasma. A digital pressure gauge (Omega DPG-500) attached to the cell allows pressures in the range of 7 to 150 psi to be read. There are two ports on the cell. The outlet port is attached to a vacuum gauge and through a needle valve control to a roughing pump via a liquid nitrogen trap or to a molecular diffusion pump for completely purging and cleaning the cell. The inlet port is attached through a cold trap and needle valve to a regulator and gas bottle. Research grade gases with < 30 ppm impurities were used. Our early experiments indicated that it is important to take considerable care to remove impurities from the cell and gas lines as these may influence the breakdown thresholds and the behavior of the breakdown.[20] In addition, because the accumulation of metastable states can also influence breakdown, in all experiments the gas was circulated away from the focal volume by letting gas in through one port and out through the other.

The transmitted laser beams are recollimated as they emerge from the cell and the dye laser probe pulses are separated by a dispersion prism and aperture and are eventually focused onto a fast photodiode (Antel AR-S2).

If there is no plasma present, this photodiode simply sees a train of dye laser pulses at a repetition rate of 76 MHz. However, when the regenerative amplifier is turned on, every 20 ms a plasma is formed and the dye laser pulse which arrives at this time (the *diagnostic* pulse) is absorbed, as shown schematically in Figure 2. Because fluctuations in the dye laser power occur on a time-scale no faster than tens of milliseconds, the pulse that arrives immediately prior to the formation of the plasma can be used as an accurate *reference* for the measurement of the transmission ratio of the plasma. Thus, as shown in Figure 1, the signal from the fast photodiode is split at a 50 Ω power splitter and is directed to two separate channels of a boxcar integrator (Princeton Applied Research 4402 with 4422 integrators). The boxcar is triggered by the sync-output pulse from the regenerative amplifier and is used in static gate mode with 2 ns windows and time delays

set to capture the amplitude of the *diagnostic* pulse in channel 1 and that of the *reference* pulse in channel 2. In addition, the amplitude of the photodiode pulse which monitors the pulse energy of the regenerative amplifier is recorded in channel 3.

The time delay of the dye laser pulses with respect to the regenerative amplifier pulse can be changed by an adjustable optical delay line, using a motorized translator (Burleigh 7000/IW-712). As shown in Figure 1, a compensating delay is used so that pulses from the fast photodiode always arrive at the boxcar with the same time delay with respect to the trigger signal. The translator is programmed to take 2 ps (0.3 mm) steps and at each step the plasma transmission ratio from five breakdown pulses is averaged. The final result is obtained as the average of four bi-directional scans of the translator, with a 1 ps delay offset between the forward and backward scans.

In order to find the position of the translator for which there is zero *absolute* time delay between the dye laser diagnostic pulse and the center of the breakdown pulse (as shown in the inset in Figure 2), the cross-correlation of the two beams is measured using a non-linear crystal. The regenerative amplifier is considerably attenuated and 10 % of the 532 nm beam together with 80 % of the dye laser beam, obtained from the opposite output of the quartz substrate beamsplitter, are combined at a KDP (71° cut) crystal, which is angle-tuned so as to obtain the sum frequency. The same data acquisition and averaging scheme used to collect the pump and probe data is also used to obtain the cross-correlation function, except that the photomultiplier which measures the sum-frequency signal gives relatively slow microsecond output pulses so that a 1 μs gate width is used on the boxcar integrator. As the translator scans, the cross-correlation between the ($<$ 1 ps) dye laser pulses and the 532 nm pulses is obtained, as shown in Figure 3. A gaussian fit to this curve allows the position of the translator corresponding to zero delay to be determined. It also yields the pulse width of the 532 nm pulse as 58 ps FWHM.

Temporal jitter and short term drift between the 532 nm pulses and the dye laser pulses also contribute to the width of the cross-correlation signal. Moreover, such effects determine the time resolution of the pump and probe experiments. They are due largely to cummulative pulse shaping effects in the operation of the synchronously pumped dye laser, and are ultimately caused by intensity fluctuations of the pump laser.[21] This was measured

to be < 2 % rms and the temporal jitter and drift over the course of a single experiment are estimated to be no more than a few picoseconds rms. However, over a longer period of time, the zero delay point is found to drift by up to 20 ps, most probably due to a drift in the pump laser intensity. For this reason, in order to accurately measure and compare the absolute initiation times for breakdown under different conditions, the cross-correlation between the laser pulses is collected before and after each 6 minute experimental run.

Experiments are performed with helium, argon and nitrogen, over a range of pressures from a few torr to several atmospheres, for probe wavelengths from 560 to 600 nm and over a range of 532 nm pulse energies, corresponding to peak intensities from 10^{13} to $2 \times 10^{14} W cm^{-2}$.

In addition to measuring the 'rise-time' of the plasma in each pump and probe experiment, the relaxation time of the plasma was also recorded by collecting the amplitude of dye laser pulses subsequent to the diagnostic pulse. This was achieved by using the boxcar in waveform mode. All data acquisition was automated by controlling the boxcar and translator controller by a personal computer.

III. Experimental Conditions

The beam mode of the 532 nm pulses is a close to Gaussian, so that the intensity near focus may approximately be expressed in cylindrical coordinates as

$$I(r,z,\theta,t) = \hat{I}\, \exp[-t'^2/2\sigma_t^2]\ \exp[-2r^2/\omega_0^2(1+a^2z^2)]/(1+a^2z^2), \qquad (1)$$

where $t' = t - z/c$, $\hat{I} = E/(\sigma_t\sqrt{2\pi}\frac{\pi}{2}\omega_0^2)$ is the peak intensity, E is the pulse energy, $\sigma_t = \mathrm{FWHM}/2\sqrt{2\ln 2}$ where FWHM= $58ps$ is the pulsewidth, $\omega_0 = 7.8\ \mu m$ is the beam waist, and $1/a = \pi\omega_0^2/\lambda = 0.36\ mm$ is the Rayleigh length.

Because the beam waist is considerably smaller than the Rayleigh length and because intensity falls exponentially ($\exp(-r^2)$) in the radial direction but only quadratically (z^{-2}) in the axial direction, the effective volume of the breakdown region is expected to be a long thin cylindrical shape, as shown in Figure 4. By arranging the probe beam to be collinear to the 532 nm beam, the probe pulses sweep through the full length of the breakdown region and are a sensitive indication of the presence of the plasma. Indeed, as the pressure

inside the cell is gradually increased so as to allow the formation of a plasma, the probe pulses show some absorption even when the plasma is not strong enough to be visible through the viewing window.

One disadvantage of this collinear optical configuration is that the interaction of the probe pulses is quite dependent on alignment, so that the response is dependent on the pointing stability of the lasers and of the optical delay line. By averaging the transmission ratio over many laser pulses and scans of the optical delay line the effects of jitter in the pointing alignments of the lasers are somewhat averaged.

Note also that the transit time of a light pulse through this long breakdown region is longer than the lengths of the pulses, and for each plasma event the pump and probe pulses simultaneously sweep through the region with a fixed time delay.

The maximum pressure used is 7350 torr, and if at this pressure all atoms were singly ionized yielding an electron density of $n_e = 2.4 \times 10^{20}\ cm^{-3}$, the plasma frequency would be $\omega_{pe} = (4\pi n_e e^2/m)^{1/2} = 8.7 \times 10^{14}\ s^{-1}$, whereas the frequency of the laser pulses is $\omega > 3.1 \times 10^{15}\ s^{-1}$. Thus all experiments are performed in the regime with ω above the critical damping frequency. Also the velocity of radiation propagation in the plasma under these conditions is expected to be $v = (1 - \omega_{pe}^2/\omega^2)^{1/2}\, c = 0.96\, c$ so that even if the boundary of the plasma were abrupt, the reflection coefficient from this index boundary would be quite small. (This is still true when an upper limit for the imaginary part of the refractive index is included in the calculation of the reflection coefficient.) Thus the major causes for the attenuation of the probe pulses are expected to be absorption within the bulk of the plasma, and diffraction of the probe pulses from the long thin structure.

In most of our experiments, absorption of the probe pulses within the plasma is expected to be due mainly to inverse Bremsstrahlung, whereby incident radiation induces electronic oscillations which are damped by electron-ion collisions. If local thermal equilibrium prevails, this yields an absorption coefficient of

$$\alpha = (\omega_{pe}/\omega)^2\, (\nu_{ei}/v)\ , \tag{2}$$

where ν_{ei} is the electron-ion collision frequency, which may be obtained[3] as

$$\nu_{ei} \approx 1.36 \times 10^{-5}\, n_e/T_e^{3/2}\ \ln(2.4 \times 10^{20}\, T_e/n_e)\ , \tag{3}$$

where n_e is given in cm^{-3} and the electronic temperature, T_e, is given in eV. If thermal equilibrium does not prevail, the absorption coefficient α must be computed from the energy distribution function of the free electrons.

V. Results and Discussion

In Figure 5 we show the transmission ratio of 590 nm probe pulses due to the breakdown in Nitrogen gas at a pressure of 50 torr for a range of 532 nm pulse energies. The initiation time of the plasma is seen to occur at earlier times for larger pulse energies. The rate of growth of the plasma as indicated by the rate of change of the transmission ratio is seen to be larger for larger pulse energies. Also, the transmission ratio is seen to continue to fall for times after the breakdown pulse has passed, indicating that the plasma continues to grow due to its internal energy rather than externally supplied energy.

In Figure 6 we show the transmission ratio of 590 nm probe pulses due to the breakdown in nitrogen gas for a 532 nm pulse energy of 9.5 mJ over a range of pressures up to 3670 torr. At the lower pressures the plasma continues to grow after the breakdown pulse has passed. Even for a pressure as low as 0.1 torr, some decrease in the transmission ratio of the probe pulse is seen hundreds of picoseconds after the breakdown pulse has passed. At this pressure and at a pressure of 1 torr, the plasma was not visible. That this change in the transmission ratio is due to a phenomena within the nitrogen rather than a nonlinear effect at the cell windows or other optics is demonstrated by the absence of change when the cell was completely evacuated.

For a pressure of 0.1 torr of N_2, the electron-neutral collision frequency which determines the rate of growth of the plasma due to cascade ionization, can be estimated for a given electron temperature and density. If we assume an electronic temperature of $T_e = 1\ eV$, and an electron density of $6.4 \times 10^{15}\ cm^{-3}$ (all N atoms singly ionized), we find $\nu_e = 0.9\ ps^{-1}$. Thus it is quite reasonable to expect that a condition of non-equilibrium persists and that this is responsible for the continued growth of the plasma after the breakdown pulse has passed. The production of the first energetic electrons is expected to be due to multiphoton ionization caused by the breakdown pulse.

In Figure 6, as the pressure is increased, the rate of growth of the plasma increases and the initiation time of the plasma moves to earlier times. At a pressure of 3670 torr,

we see a 66 % change in transmission ratio over a time-scale of only 20 ps, whereas the breakdown pulse has a width of $2\sigma_t = 50\ ps$ (FWHM = 58 ps), i.e., the breakdown is considerably faster than the 532 nm pulse.

The temporal characteristics of the breakdown in argon appear similar to that in nitrogen, although the pressure or pulse energy required to get breakdown is higher. The transmission ratio of 590 nm probe pulses for breakdown in argon is shown firstly at a pressure of 1570 torr and for a range of 532 nm pulse energies in Figure 7, and secondly over a range of pressures up to 1500 torr, for a 532 nm pulse energy of 10.3 mJ in Figure 8.

Breakdown in helium was only found to occur at higher pulse energies and pressures. We were not able to observe the very weak absorption of the probe pulses which occurs after the breakdown pulse has passed and which initiates in the trailing edge of the breakdown pulse. Figure 8 shows the transmission ratio versus delay of a 590 nm probe pulse through a helium plasma caused by a 9.5 mJ 532 nm pulse over a range of pressures. At the higher pressures the growth of the plasma is seen to be quite abrupt, consistent with the expectation that growth proceeds by cascade ionization under these conditions.

Experiments were performed over a range of dye laser probe wavelengths for a fixed 532 nm pulse energy and gas pressure. These experiments did not detect an appreciable change in the *shape* of the curves of the transmission ratio versus delay, but in general, the absorption of the probe pulses was found to be considerably greater at longer wavelengths. Equation (2) gives an absorption coefficient proportional to $((\omega/\omega_{pe})^4 - 1)^{-1/2}$, so that for inverse Bremsstrahlung, greater absorption is expected at longer wavelengths. Figure 10 shows the case of breakdown in helium probed at four different wavelengths. Here we find that the probe pulse absorption increases steadily as the wavelength is increased, except for a sharp peak in absorption at 587 nm, which corresponds to the $2p^3P^0 \rightarrow 3d^3D$ transition in the spectrum of neutral Helium. At 587 nm the absorption is about the same as that at 590 nm, whereas at 585 nm the absorption is found to be about midway between that at 580 nm and that at 590 nm.

In addition to measuring the transmission ratios versus delay, at each condition of pressure, breakdown pulse energy and different gas type, the waveform from the dye laser

pulses is collected out to 200 ns following breakdown. From the change in the absorption of the dye laser probe pulses over this period, we can monitor the relaxation of the plasma. For all three gases, the relaxation time is found to be approximately linearly dependent on pressure and may be as short as 10 ns or longer than 100 ns.

Figure 11 shows the waveform collected from a helium plasma at moderate pressure showing an incomplete recovery of the plasma in a time of about 50 ns. While some of the pulse-to-pulse fluctuations of the transmitted dye laser pulses shown in this waveform are due to radio-frequency pick-up of noise from the regenerative amplifier flashlamp discharge, most of the fluctuations are found to be critically dependent on the collinear alignment of the pump and probe laser beams. If this alignment is deliberately misadjusted, clear oscillations in the transmission of the dye laser probe pulses can be seen. This is possibly due to refractive loss of the probe beam from the shock wave emanating from the breakdown region. Such effects would make quantitative measurements of the relaxation of the plasma absorption by this method very difficult.

Nevertheless, qualitative features of the plasma relaxation can be discerned. In the case of helium plasmas, when the probe pulse wavelength is changed to 587 nm, corresponding to the $2p^3P^0 \rightarrow 3d^3D$ transition, as shown in Figure 12, the absorption of the probe pulses continues to increase for about 10 ns and while the time constant for the relaxation of the probe pulse absorption is about the same, the residual absorption after 200 ns is greater. This residual absorption is probably due to the presence of metastable states which relax to the $2p^3P^0$ state.

IV. Conclusions

We have used a collinear pump and probe technique to measure the temporal response of laser breakdown plasmas in nitrogen, argon and helium, with a resolution of a few picoseconds. The high f-number focusing geometry used, results in a long thin plasma which gives high sensitivity to the absorption of the probe pulses by the plasma but which has the disadvantage that the response of the probe pulses is dependent on exact collinear beam alignment.

Several features in the temporal response of the breakdown and plasma growth have been noted For example, at low pressures in argon and nitrogen, growth of the plasma

continues after the breakdown pulse has passed, while at high pressures, in all gases, the breakdown is seen to be quite abrupt compared to the duration of the breakdown pulse. The relaxation time of the plasma absorption was also measured and this is found to be pressure dependent with a half-life of up to 100 *ns* for a pressure of several atmospheres.

References

1. R.W. Terhune, "Third International Symposium on Quantum Electronics," Paris, Feb., 1963.
2. E.K. Damon and R.G. Tomlinson, Appl. Opt. **2**, 546 (1963).
3. G.M. Weyl, "Physics of Laser-Induced Breakdown: An Update", pp. 1– 67 in *Laser-Induced Plasmas and Applications*, ed. by L.J. Radziemski and D.P. Cremers, Marcel Dekker, 1989; and references therein.
4. C. Grey Morgan, Rep. Prog. Phys. **38**, 621 (1975).
5. P. Agostini, G. Barjot, G. Mainfray, C. Manus and J. Thebault, IEEE J. Quant. Elect. **QE-6**, 782 (1970).
6. G. Baravian, J. Godart and G. Sultan, Phys. Rev. A **25**, 1483 (1982).
7. S. Augst, D.D. Meyerhofer, D. Strickland and S.L. Chin, J. Opt. Soc. Am. B **8**, 858 (1991).
8. Y.E. Gamal and M. A. Harith, J. Phys. D: Appl. Phys. **16**, 1901 (1983).
9. R.W. Minck, J. App. Phys. **35**, 252 (1964).
10. R.J. Dewhurst, J. Phys. D: App. Phys. **11**, 191 (1978).
11. E.W. Van Stryland, M.J. Soileau, A.L. Smirl and W.E. Williams, Phys. Rev. B **23**, 2144 (1981).
12. G.M. Weyl and D. Rosen, Phys. Rev. A **31**, 2300 (1985).
13. D.I. Rosen and G. Weyl, J. Phys D: Appl. Phys. **20**, 1264 (1987).
14. N. Kroll and K.M. Watson, Phys. Rev. A **5**, 1883 (1972).
15. A.V. Phelps, "Theory of Growth of Ionization During Laser Breakdown," pp. 538–547 in *Physics of Quantum Electronics*, ed. by P. Kelley, B. Lax, P. Tannenwald (1966).
16. J. Stricker and J.G. Parker, J. App. Phys. **53**, 851 (1982).
17. R.A. Armstrong, R.A. Lucht and W.T. Rawlins, Appl. Opt. **22**, 1573 (1983).
18. L.J. Radziemski, T.R. Loree, D.A. Cremers and N.M. Hoffman, Anal. Chem. **55**, 1246 (1983).
19. C.L.M. Ireland, A. Yi, J.M. Aaron and C. Grey Morgan, Appl. Phys. Lett. **24**, 175 (1974).
20. D.E. Lencioni, App. Phys. Lett. **23**, 12 (1973); ibid. **25**, 15 (1974).

21. L.M. Davis, J.D.Harvey and J.M.Peart, Opt. Comm. **50**, 49 (1984).

Figure Captions

Fig. 1 Pump and probe experiment to measure the initiation of laser induced plasmas. ($\lambda/2$ =half-wave plate, pol. = Glan-Taylor polarizer, PD = photodiode, PM = photomultiplier, ND = neutral density filter.)

Fig. 2 Timing relationship between the 532 nm breakdown pulse and the dye laser pulses.

Fig. 3 Cross-correlation between the 532 nm breakdown pulses and the dye laser *diagnostic* pulses.

Fig. 4 The effective breakdown volume (as calculated by equation (1) with $I/\hat{I} = 0.5$.) has a long thin cylindrical shape. Note that the aspect ratio of r:z has been scaled by ~~10:1~~ 100:1 in this graph.

Fig. 5 Breakdown in Nitrogen, at a pressure of 50 torr, for varying pulse energies. At the maximum pulse energy of 9.1 mJ, the peak intensity is $1.5 \times 10^{14} W\,cm^{-2}$.

Fig. 6 Breakdown in Nitrogen, at varying pressures, for a mean pulse energy of 9.5 mJ. This corresponds to a peak intensity of $1.6 \times 10^{14} W\,cm^{-2}$.

Fig. 7 Breakdown in Argon, at a pressure of 1570 torr, for varying pulse energies. At the maximum pulse energy of 7.9 mJ, the peak intensity is $1.3 \times 10^{14} W\,cm^{-2}$.

Fig. 8 Breakdown in Argon, at varying pressures, for a mean pulse energy of 10.3 mJ. This corresponds to a peak intensity of $1.7 \times 10^{14} W\,cm^{-2}$.

Fig. 9 Breakdown in Helium, at varying pressures, for a mean pulse energy of 9.5 mJ. This corresponds to a peak intensity of $1.6 \times 10^{14} W\,cm^{-2}$.

Fig. 10 Breakdown in Helium, at a pressure of 1570 torr, for a mean 532 nm pulse energy of 7.1 mJ, corresponding to a peak intensity of $1.2 \times 10^{14} W\,cm^{-2}$, as seen by

picosecond probe pulses at four different wavelengths. There is a steady increase in the absorption of probe pulses as the wavelength is increased, except at 587 nm, for which an enhanced absorption is observed.

Fig. 11 The waveform collected from breakdown in Helium, at a pressure of 1570 torr, for a pulse energy of 7.1 mJ, corresponding to a peak intensity of $1.2 \times 10^{14} W\,cm^{-2}$, using picosecond probe pulses at a wavelength of 590 nm. The plasma absorption is seen to give incomplete relaxation with a half-life of $\sim$ 50 ns.

Fig. 12 The waveform collected from breakdown in Helium, at the same conditions as in Fig. 11, but using picosecond probe pulses at a wavelength of 587 nm. The plasma absorption is seen to grow for about 10 ns after breakdown and then give incomplete relaxation with about the same half-life of $\sim$ 50 ns.

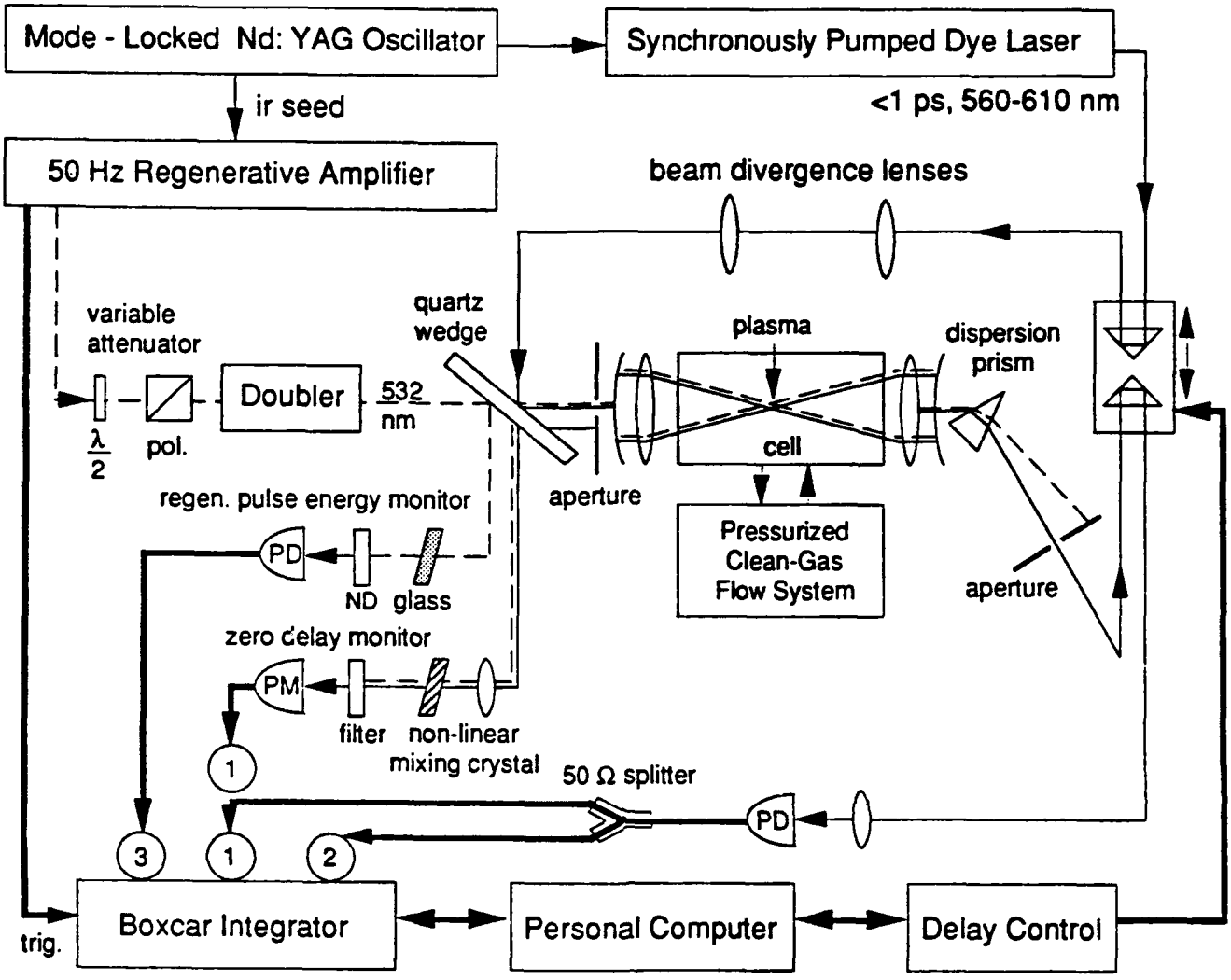
Mode - Locked Nd: YAG Oscillator
Synchronously Pumped Dye Laser
<1 ps, 560-610 nm
ir seed
50 Hz Regenerative Amplifier
beam divergence lenses
variable attenuator
quartz wedge
plasma
dispersion prism
Doubler
532 nm
λ/2
pol.
cell
aperture
Pressurized Clean-Gas Flow System
aperture
regen. pulse energy monitor
PD
ND glass
zero delay monitor
PM
filter
non-linear mixing crystal
50 Ω splitter
PD
1
3
1
2
trig.
Boxcar Integrator
Personal Computer
Delay Control

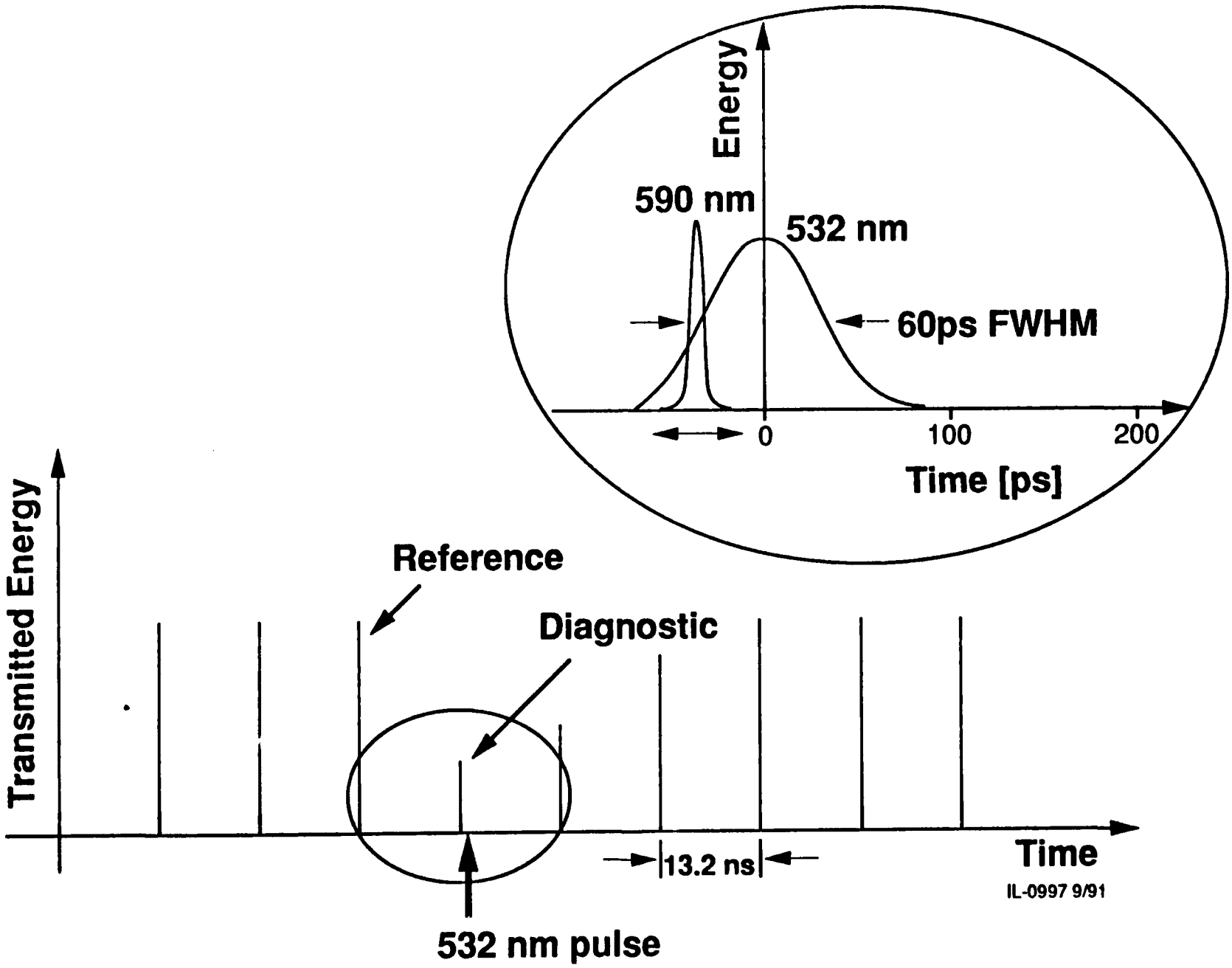
Energy
590 nm
532 nm
60ps FWHM
0
100
200
Time [ps]
Transmitted Energy
Reference
Diagnostic
13.2 ns
Time
IL-0997 9/91
532 nm pulse

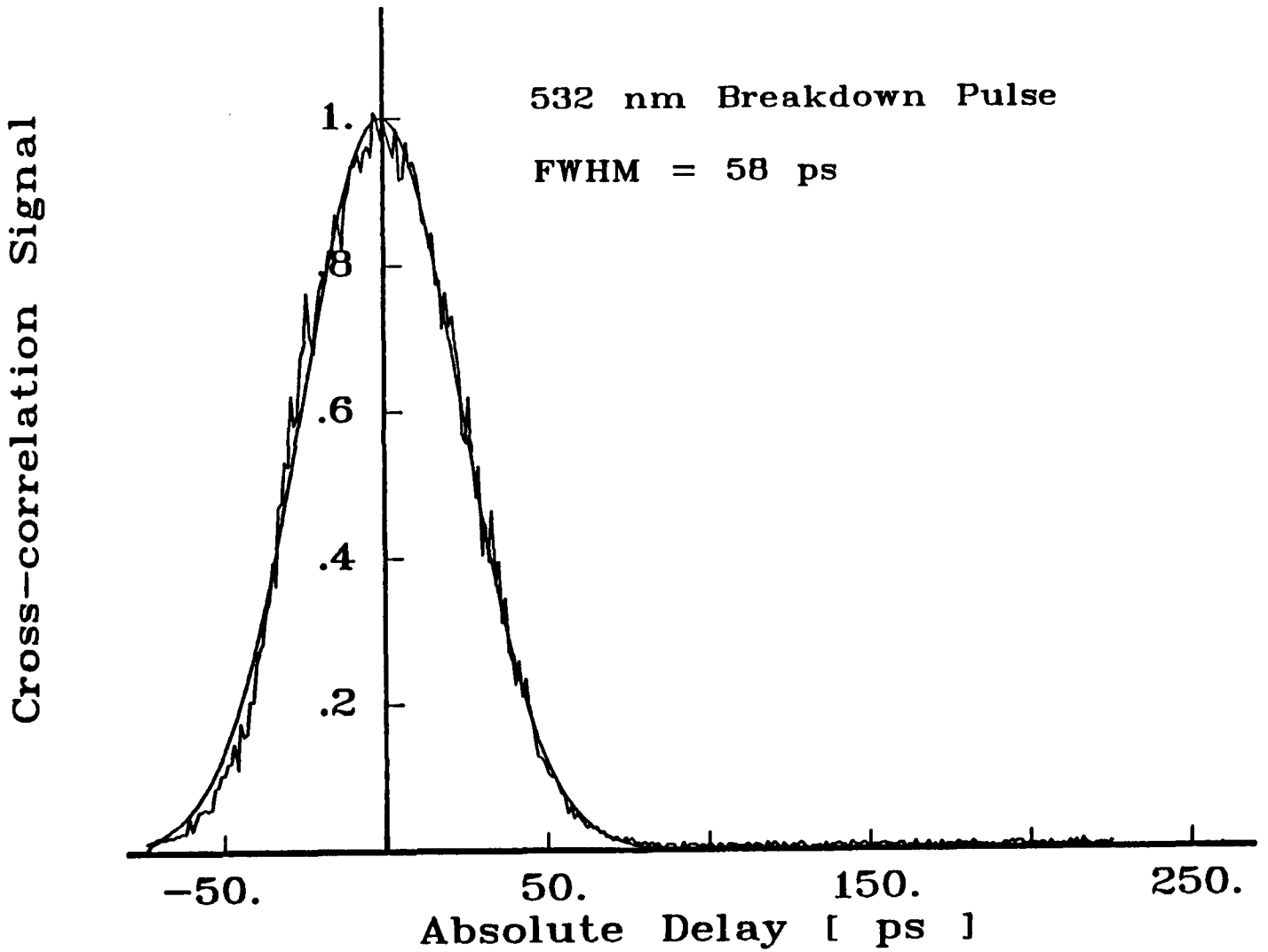
532 nm Breakdown Pulse
FWHM = 58 ps
Cross-correlation Signal
1.
.8
.6
.4
.2
-50.
50.
150.
250.
Absolute Delay [ps]

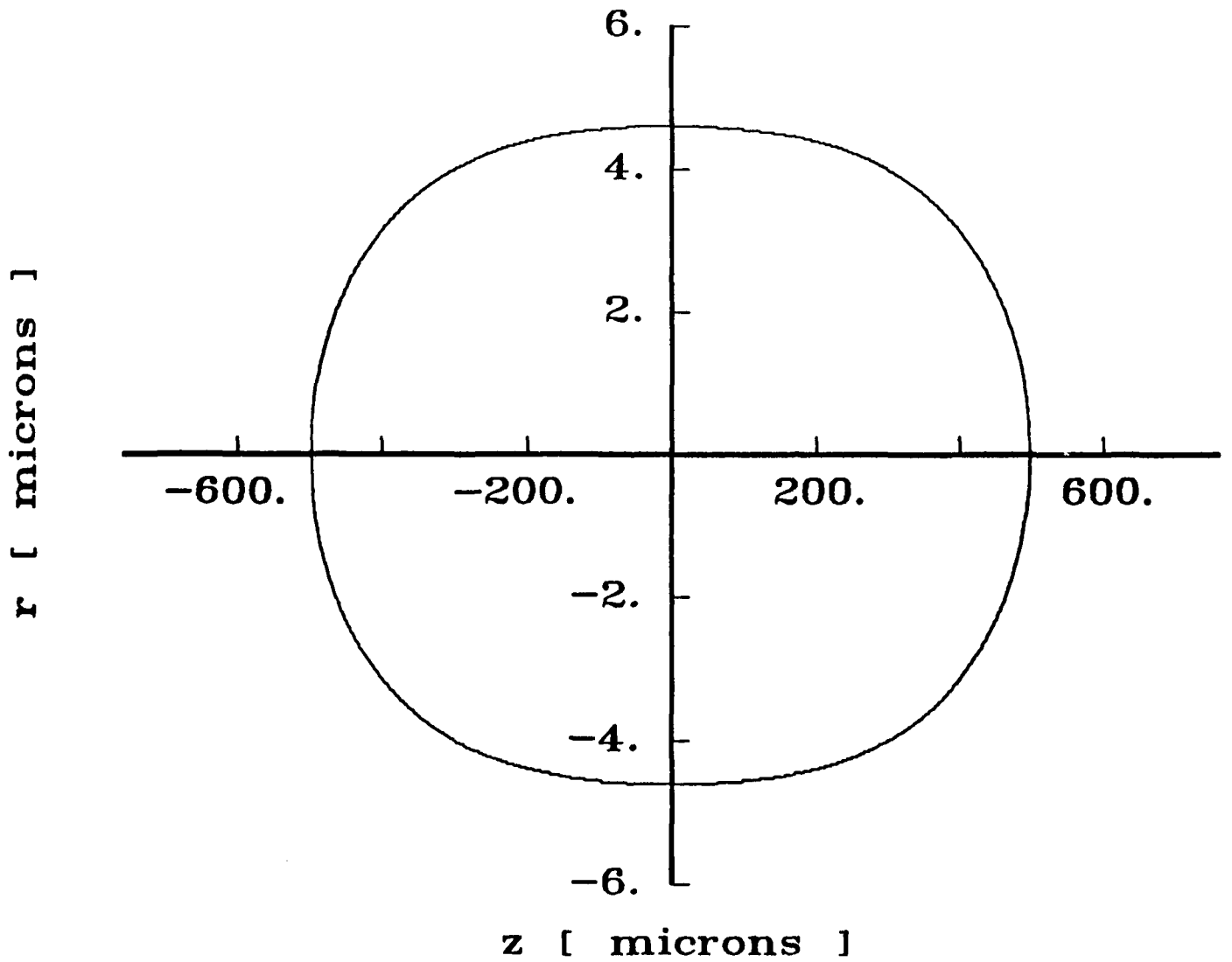
6.
4.
2.
−2.
−4.
−6.
−600.
−200.
200.
600.
r [microns]
z [microns]

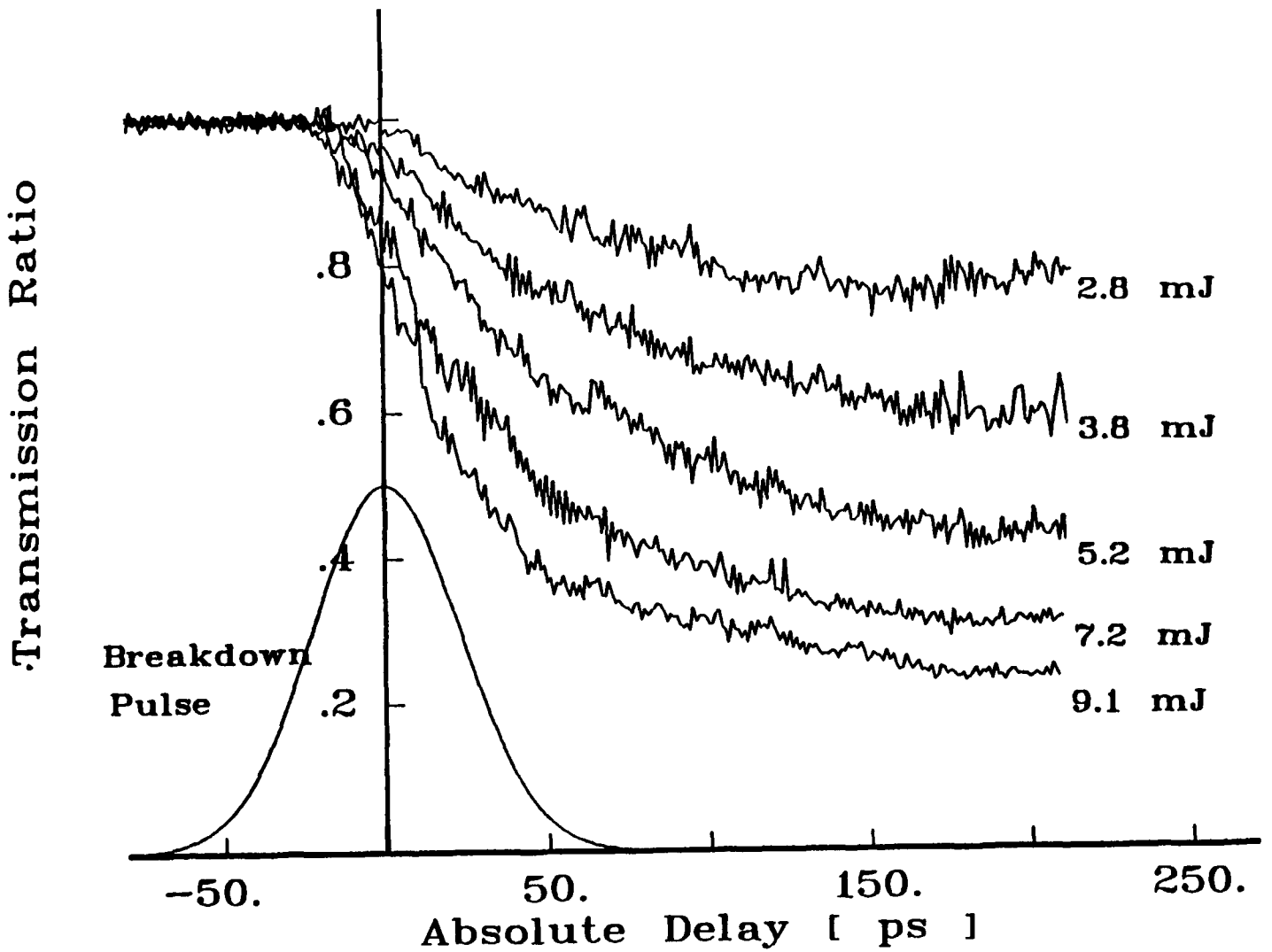
Transmission Ratio
.8
.6
.4
.2
Breakdown
Pulse
2.8 mJ
3.8 mJ
5.2 mJ
7.2 mJ
9.1 mJ
-50.
50.
150.
250.
Absolute Delay [ps]

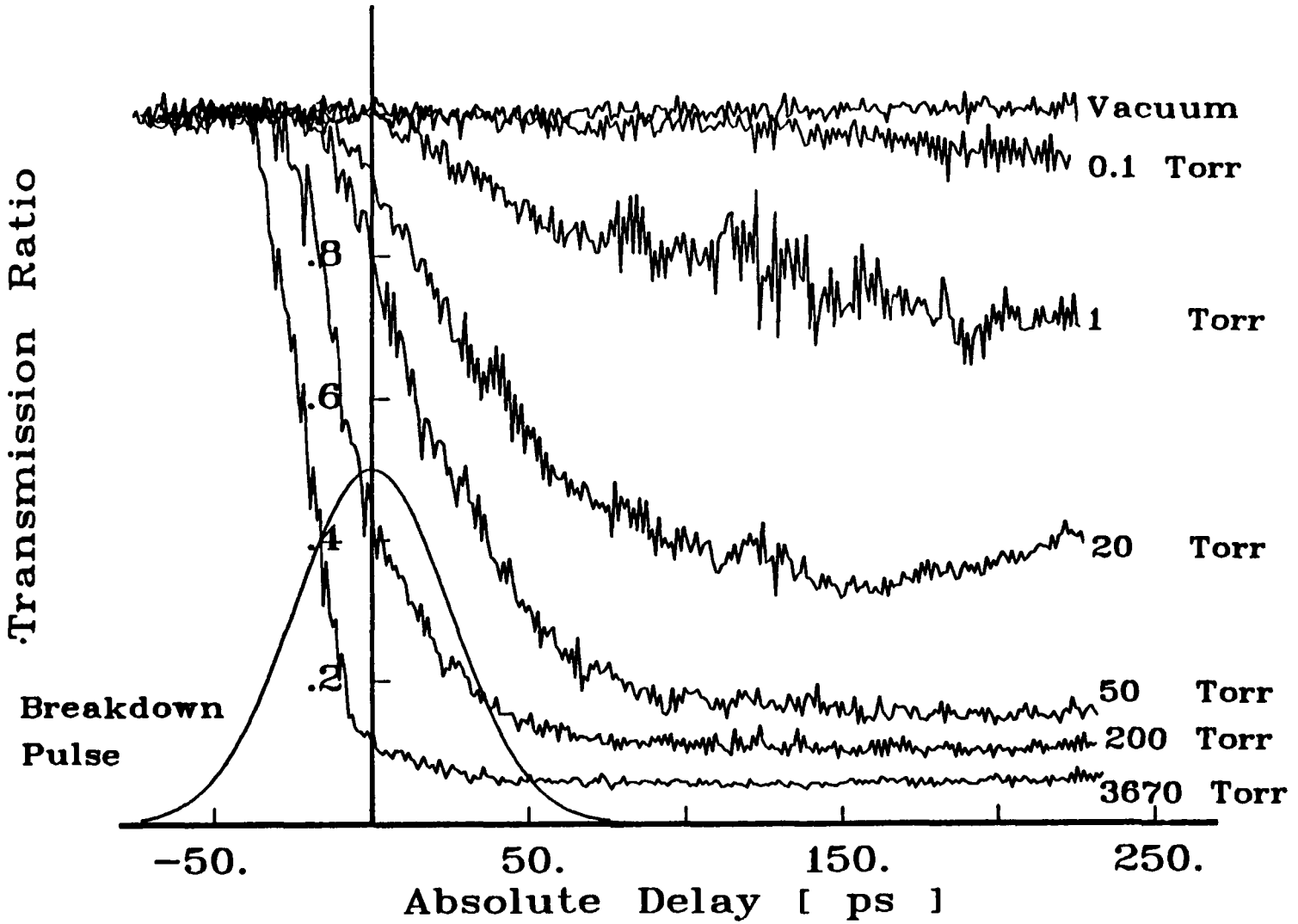
Transmission Ratio
.8
.6
.4
.2
Vacuum
0.1 Torr
1 Torr
20 Torr
50 Torr
200 Torr
3670 Torr
Breakdown
Pulse
-50.
50.
150.
250.
Absolute Delay [ps]

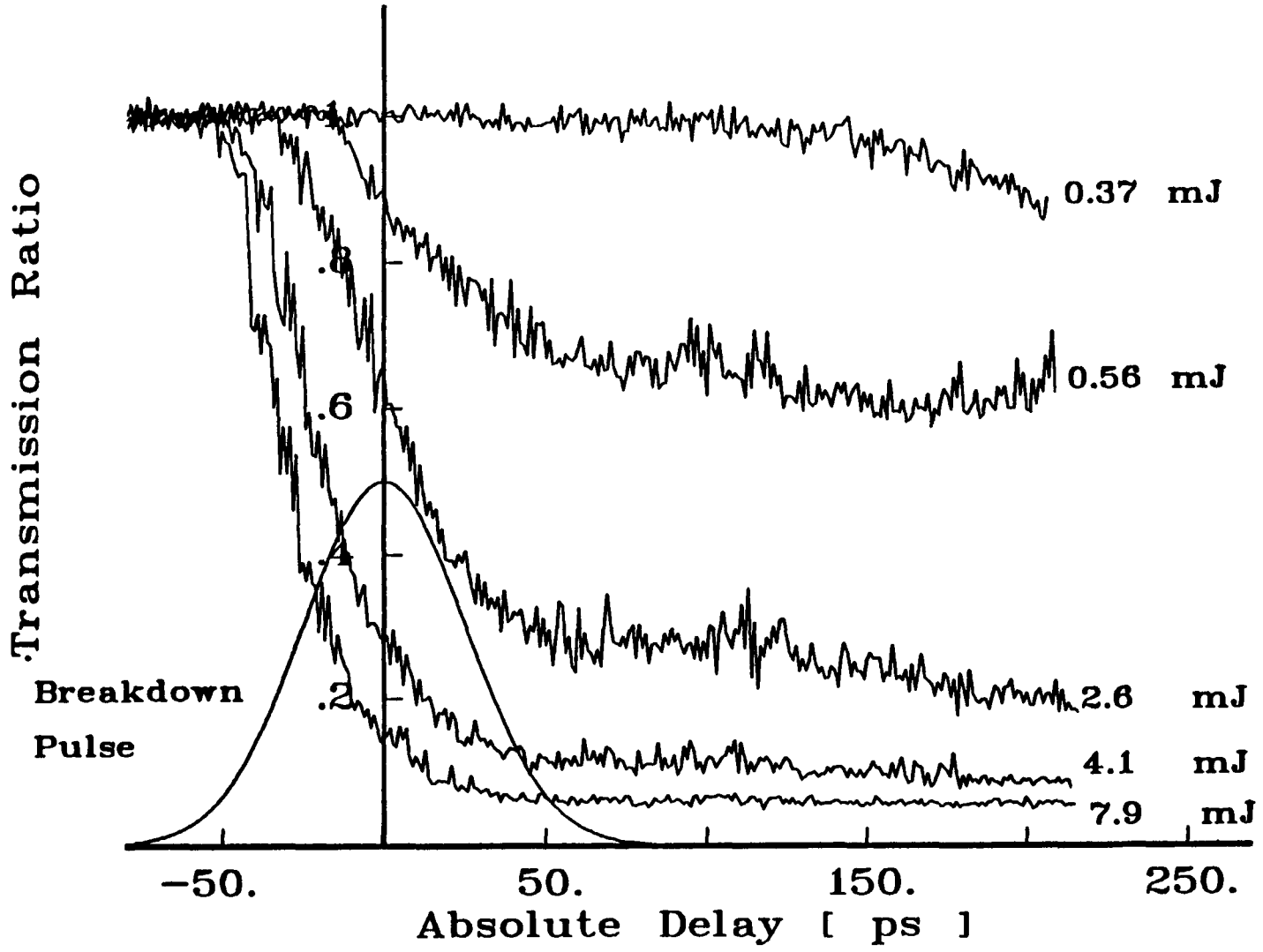
Transmission Ratio
.8
.6
.4
.2
Breakdown
Pulse
0.37 mJ
0.56 mJ
2.6 mJ
4.1 mJ
7.9 mJ
−50.
50.
150.
250.
Absolute Delay [ps]

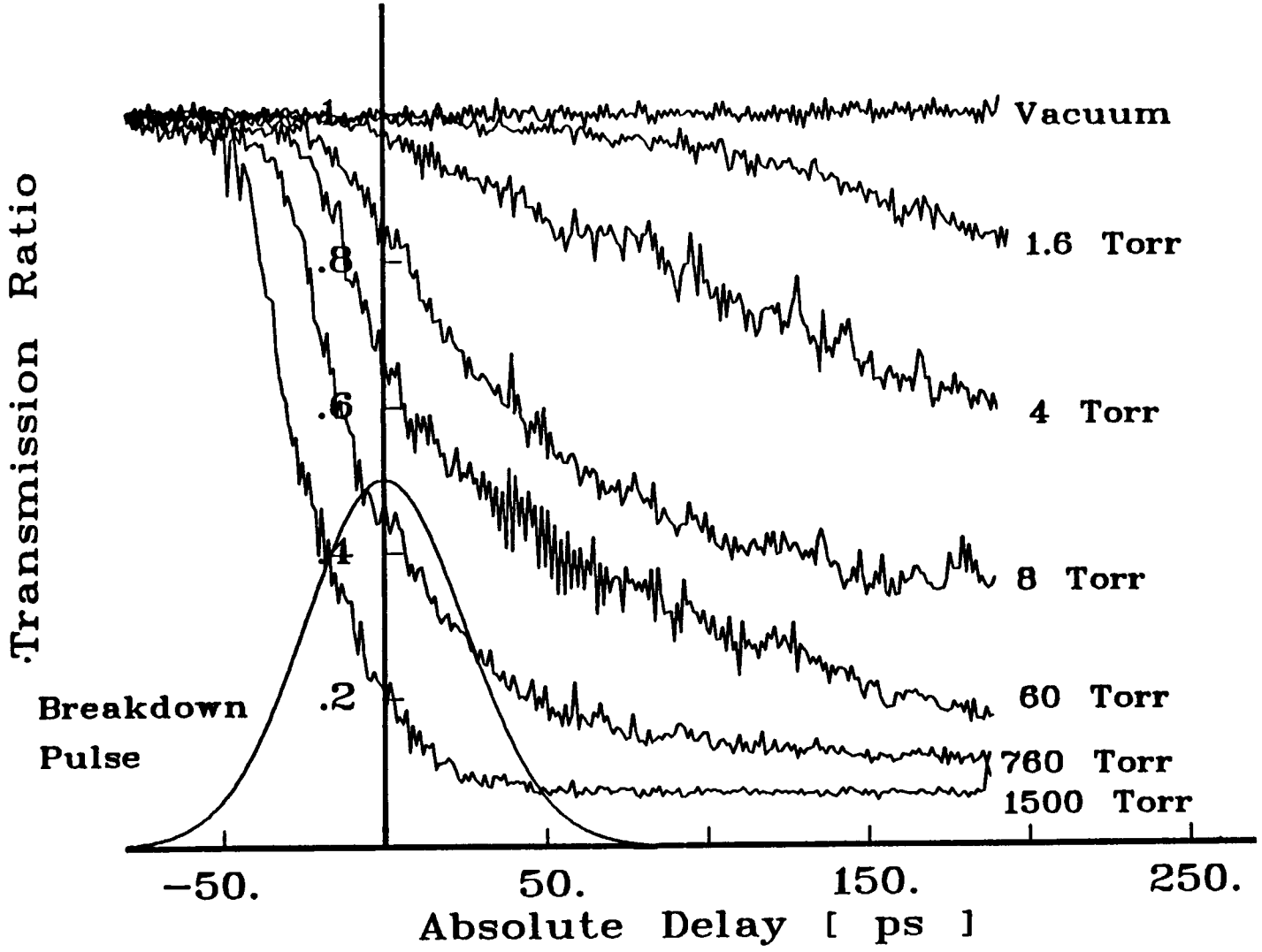
Transmission Ratio
1
.8
.6
.4
.2
Vacuum
1.6 Torr
4 Torr
8 Torr
60 Torr
760 Torr
1500 Torr
Breakdown
Pulse
-50.
50.
150.
250.
Absolute Delay [ps]

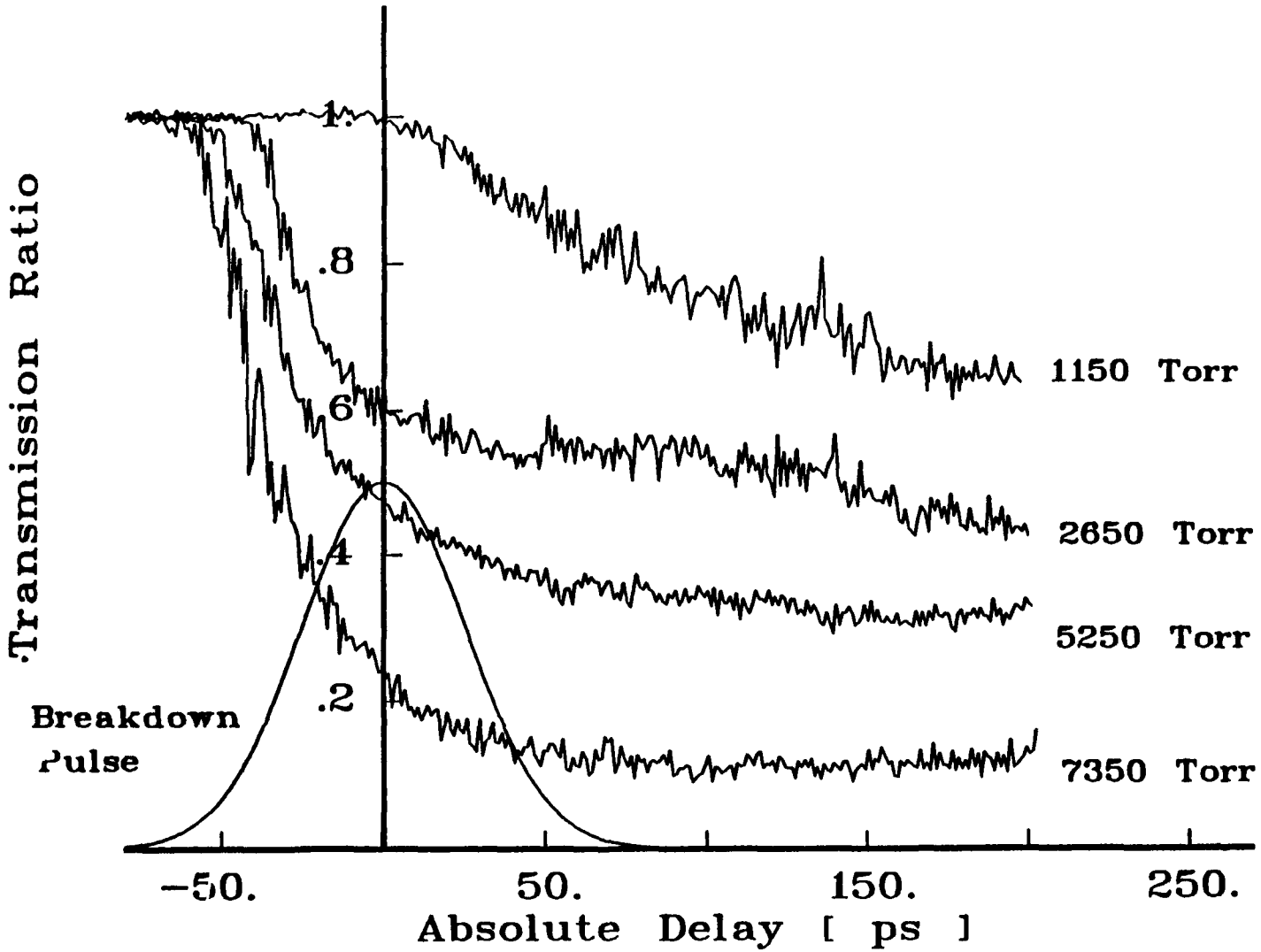
Transmission Ratio
1.
.8
.6
.4
.2
Breakdown
Pulse
1150 Torr
2650 Torr
5250 Torr
7350 Torr
-50.
50.
150.
250.
Absolute Delay [ps]

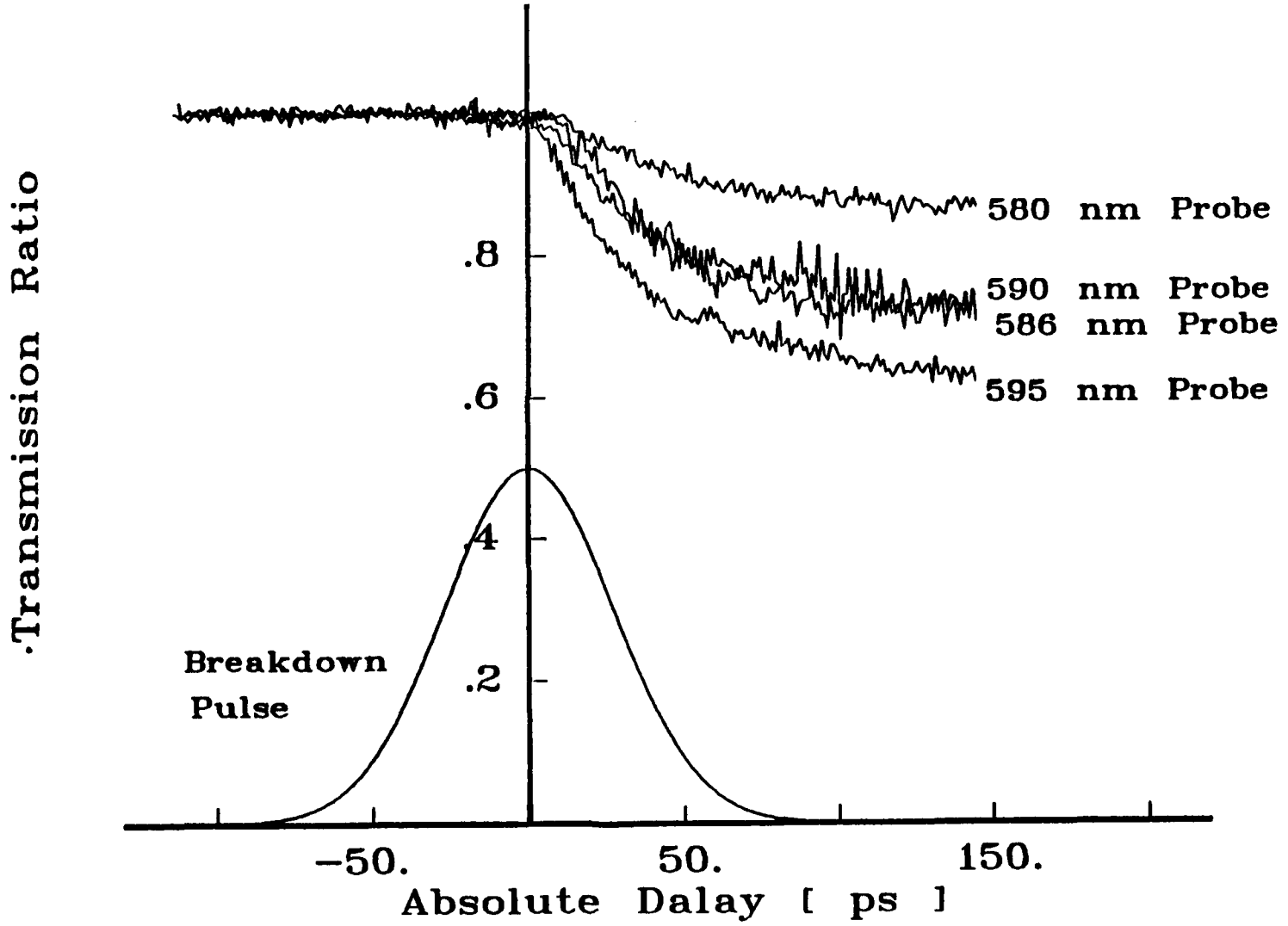
Transmission Ratio
.8
.6
.4
.2
580 nm Probe
590 nm Probe
586 nm Probe
595 nm Probe
Breakdown
Pulse
-50.
50.
150.
Absolute Dalay [ps]

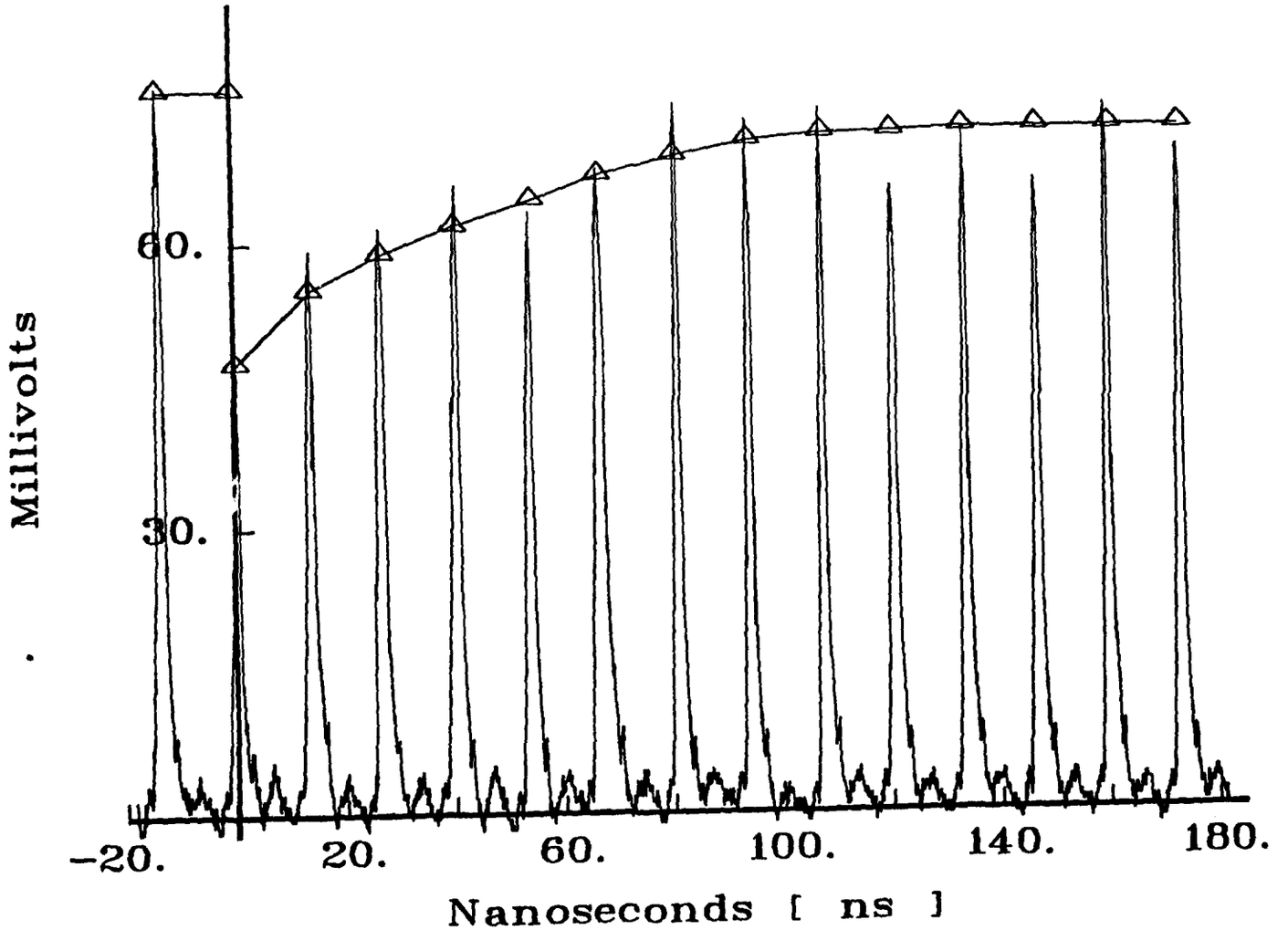
Millivolts
60.
30.
-20.
20.
60.
100.
140.
180.
Nanoseconds [ns]

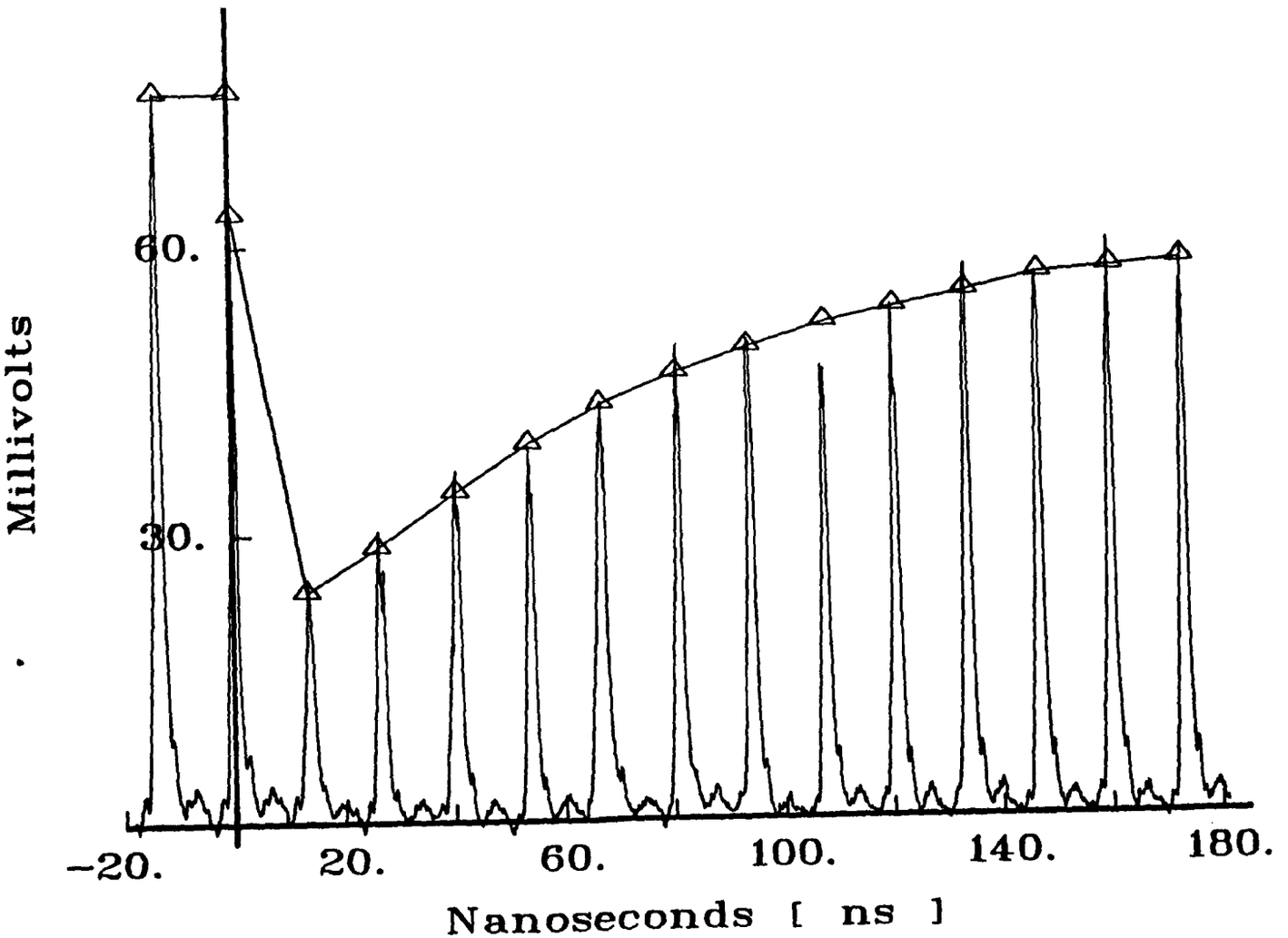
Millivolts
60.
30.
-20.
20.
60.
100.
140.
180.
Nanoseconds [ns]